

The Kernel Polynomial Method

Alexander Weiße,¹ Gerhard Wellein,² Andreas Alvermann,³ and Holger Fehske³

¹*School of Physics, The University of New South Wales, Sydney, NSW 2052, Australia*

²*Regionales Rechenzentrum Erlangen, Universität Erlangen, 91058 Erlangen, Germany*

³*Institut für Physik, Ernst-Moritz-Arndt-Universität Greifswald, 17487 Greifswald, Germany*

(Dated: April 25, 2005)

Efficient and stable algorithms for the calculation of spectral quantities and correlation functions are some of the key tools in computational condensed matter physics. In this article we review basic properties and recent developments of Chebyshev expansion based algorithms and the Kernel Polynomial Method. Characterised by a resource consumption that scales linearly with the problem dimension these methods enjoyed growing popularity over the last decade and found broad application not only in physics. Representative examples from the fields of disordered systems, strongly correlated electrons, electron-phonon interaction, and quantum spin systems we discuss in detail. In addition, we illustrate how the Kernel Polynomial Method is successfully embedded into other numerical techniques, such as Cluster Perturbation Theory or Monte Carlo simulation.

Contents

I. Introduction	1	IV. KPM as a component of other methods	21
II. Chebyshev expansion and the Kernel Polynomial Method (KPM)	3	A. Monte Carlo simulations	21
A. Basic features of Chebyshev expansion	3	B. Cluster Perturbation Theory (CPT)	22
1. Chebyshev polynomials	3	1. General features of CPT	22
2. Modified moments	3	2. CPT for the Hubbard model	23
B. Calculation of moments	4	3. CPT for the Holstein model	24
1. General considerations	4	V. Overview of alternatives to KPM	24
2. Stochastic evaluation of traces	5	A. Chebyshev expansion and Maximum Entropy methods	24
C. Kernel polynomials and Gibbs oscillations	6	B. Lanczos recursion	24
1. Expansions of finite order & simple kernels	6	C. Projection methods	26
2. Jackson kernel	7	D. Forced Oscillator Method	26
3. Lorentz kernel	8	VI. Conclusions & Outlook	26
D. Implementational details and remarks	9	Acknowledgements	26
1. Discrete cosine & Fourier transforms	9	References	27
2. Integrals involving expanded functions	10		
E. Generalisation to higher dimension	10		
1. Expansion of multivariate functions	10		
2. Kernels for finite order expansions	10		
3. Reconstruction with cosine transforms	11		
III. Applications of KPM	11		
A. Densities of states	11	I. INTRODUCTION	
1. General considerations	11		
2. Non-interacting systems: Anderson model of disorder	12		
3. Interacting systems: Double exchange	13		
B. Dynamical correlation functions at $T = 0$	14		
1. General considerations	14		
2. One-particle spectral function	14		
3. Optical conductivity	16		
4. Spin structure factor	16		
C. Static correlations at $T > 0$	17		
D. Dynamical correlations at finite temperature	18		
1. General considerations	18		
2. Optical conductivity of the Anderson model	19		
3. Optical conductivity of the Holstein model	20		

In most areas of physics the fundamental interactions and the equations of motion that govern the behaviour of real systems on a microscopic scale are very well known, but when it comes to solving these equations they turn out to be exceedingly complicated. This holds, in particular, if a large and realistic number of particles is involved. Inventing and developing suitable approximations and analytical tools has therefore always been a cornerstone of theoretical physics. Recently, however, research continued to focus on systems and materials, whose properties depend on the interplay of many different degrees of freedom or on interactions that compete on similar energy scales. Analytical and approximate methods quite often fail to describe the properties of such systems, so that the use of numerical methods remains the only way to proceed. On the other hand, the available computer power increased tremendously over

the last decades, making direct simulations of the microscopic equations for reasonable system sizes or particle numbers more and more feasible. The success of such simulations, though, depends on the development and improvement of efficient algorithms. Corresponding research therefore plays an increasingly important role.

On a microscopic level the behaviour of most physical systems, like their thermodynamics or response to external probes, depends on the distribution of the eigenvalues and the properties of the eigenfunctions of a Hamilton operator or dynamical matrix. In numerical approaches the latter correspond to Hermitian matrices of finite dimension D , which can become huge already for a moderate number of particles, lattice sites or grid points. The calculation of all eigenvalues and eigenvectors then easily turns into an intractable task, since for a D -dimensional matrix in general it requires memory of the order of D^2 and the number of operations and the computation time scale as D^3 . Of course, this large resource consumption severely restricts the size of the systems that can be studied by such a “naive” approach. For dense matrices the limit is currently of the order of $D \approx 10^5$, and for sparse matrices the situation is only slightly better.

Fortunately, alternatives are at hand: In the present article we review basic properties and recent developments of numerical Chebyshev expansion and of the Kernel Polynomial Method (KPM). As the most time consuming step these iterative approaches require only multiplications of the considered matrix with a small set of vectors, and therefore allow for the calculation of the spectral properties and of dynamical correlation functions with a resource consumption that scales *linearly* with D for sparse matrices, or like D^2 otherwise. If the matrix is not stored but constructed on-the-fly dimensions of the order of $D \approx 10^9$ or more are accessible.

The first step to achieve this favourable behaviour is setting aside the requirement for a complete and exact knowledge of the spectrum. A natural approach, which has been considered from the early days of quantum mechanics, is the characterisation of the spectral density $\rho(E)$ in terms of its moments $\mu_l = \int \rho(E) E^l dE$. By iteration these moments can usually be calculated very efficiently, but practical implementations in the context of Gaussian quadrature showed that the reconstruction of $\rho(E)$ from ordinary power moments is plagued by substantial numerical instabilities [1]. These occur mainly because the powers E^l put too much weight to the boundaries of the spectrum at the expense of poor precision for intermediate energies. The observation of this deficiency advanced the development of so-called modified moment approaches [2, 3], where E^l is replaced by (preferably orthogonal) polynomials of E . With studies of the spectral density of harmonic solids [4, 5, 6] and of autocorrelation functions [7], which made use of Chebyshev polynomials of second kind, these ideas soon found their way into physics application. Later, similar Chebyshev expansion methods became popular also in quantum chemistry, where the focus was on the time evolution of quantum

states [8, 9, 10, 11] and on the so-called Filter Diagonalisation [12]. The modified moment approach noticeably improved when kernel polynomials were introduced to damp the Gibbs oscillations, which for truncated polynomial series occur near discontinuities of the expanded function [13, 14, 15, 16]. At this time also the name Kernel Polynomial Method was coined, and applications then included high-resolution spectral densities, static thermodynamic quantities as well as zero-temperature dynamical correlations [13, 14, 15]. Only recently this range was extended to cover also dynamical correlation functions at finite-temperature [17], and below we present some new applications to complex-valued quantities, e.g. Green functions. Being such a general tool for studying large matrix problems, KPM can also be used as a core component of more involved numerical techniques. As recent examples we discuss Monte Carlo (MC) simulations and Cluster Perturbation Theory (CPT).

In parallel to Chebyshev expansion techniques and to KPM also the so-called Lanczos Recursion Method was developed [18, 19, 20, 21, 22, 23], which is based on a recursive Lanczos tridiagonalisation [24] of the considered matrix and the expression of the spectral density or of correlation functions in terms of continued fractions. The approach, in general, is applicable to the same problems as KPM and found wide application in solid state physics [25, 26, 27, 28]. It suffers, however, from the shortcomings of the Lanczos algorithm, namely loss of orthogonality and spurious degeneracies if extremal eigenstates start to converge. We will compare the two methods in section V and explain, why we prefer to use Lanczos for the calculation of extremal eigenstates and KPM for the calculation of spectral properties and correlation functions. In addition, we will comment on a two other iterative schemes with a somewhat limited application range, namely projection methods [29, 30, 31] and the Forced Oscillator Method [32]. Drawing more attention to KPM as a potent alternative to all these techniques is one of the purposes of the present work.

The outline of the article is as follows: In section II we give a detailed introduction to Chebyshev expansion and the Kernel Polynomial Method, its mathematical background, convergence properties and practical aspects of its implementation. In section III we apply KPM to a variety of problems from solid state physics. Thereby, we focus mainly on illustrating the types of quantities that can be calculated with KPM, rather than on the physics of the considered models. In section IV we show how KPM can be embedded into other numerical approaches that require knowledge of spectral properties or correlation functions, namely Monte Carlo simulation and Cluster Perturbation Theory. In section V we shortly discuss alternatives to KPM and compare their performance and precision, before summarising in section VI.

II. CHEBYSHEV EXPANSION AND THE KERNEL POLYNOMIAL METHOD (KPM)

A. Basic features of Chebyshev expansion

1. Chebyshev polynomials

Let us first recall the basic properties of expansions in orthogonal polynomials and of Chebyshev expansion in particular. Given a non-negative weight function $w(x)$ defined on the interval $[a, b]$ we can introduce a scalar product

$$\langle f|g \rangle = \int_a^b w(x) f(x) g(x) dx \quad (1)$$

between two functions $f, g : [a, b] \rightarrow \mathbb{R}$. With respect to each such scalar product there exists a set of polynomials $p_n(x)$, which fulfil the orthogonality relations

$$\langle p_n | p_m \rangle = \delta_{n,m} / w_n, \quad (2)$$

where w_n denotes the inverse of the squared norm of $p_n(x)$. These orthogonality relations allow for an easy expansion of a given function $f(x)$ in terms of the $p_n(x)$, since the expansion coefficients are proportional to the scalar products of f and p_n ,

$$f(x) = \sum_{n=0}^{\infty} \alpha_n p_n(x) \quad \text{with} \quad \alpha_n = \langle p_n | f \rangle / w_n. \quad (3)$$

In general, all types of orthogonal polynomials can be used for such an expansion and for the Kernel Polynomial approach we discuss in this article (see e.g. Ref. 13). However, as we frequently observe whenever we work with polynomial expansions [33], Chebyshev polynomials [34, 35] of first and second kind turn out to be the best choice for most applications, mainly due to the good convergence properties of the corresponding series and to the close relation to Fourier transform [36, 37]. The latter is also an important prerequisite for the derivation of optimal kernels (see section II C), which are required for the regularisation of finite-order expansions, and which so far have not been derived for other sets of orthogonal polynomials.

Both sets of Chebyshev polynomials are defined on the interval $[a, b] = [-1, 1]$, where the weight function $w(x) = (\pi\sqrt{1-x^2})^{-1}$ yields the polynomials of first kind, T_n , and the weight function $w(x) = \pi\sqrt{1-x^2}$ those of second kind, U_n . Based on the scalar products

$$\langle f|g \rangle_1 = \int_{-1}^1 \frac{f(x) g(x)}{\pi\sqrt{1-x^2}} dx, \quad (4)$$

$$\langle f|g \rangle_2 = \int_{-1}^1 \pi\sqrt{1-x^2} f(x) g(x) dx, \quad (5)$$

the orthogonality relations thus read

$$\langle T_n | T_m \rangle_1 = \frac{1+\delta_{n,0}}{2} \delta_{n,m}, \quad (6)$$

$$\langle U_n | U_m \rangle_2 = \frac{\pi^2}{2} \delta_{n,m}. \quad (7)$$

By substituting $x = \cos(\varphi)$ one can easily show that they correspond to the orthogonality relations of trigonometric functions, and that in terms of those the Chebyshev polynomials can be expressed in explicit form,

$$T_n(x) = \cos(n \arccos(x)), \quad (8)$$

$$U_n(x) = \frac{\sin((n+1) \arccos(x))}{\sin(\arccos(x))}. \quad (9)$$

These expressions can then be used to prove the recursion relations,

$$\begin{aligned} T_0(x) &= 1, & T_{-1}(x) &= T_1(x), \\ T_{m+1}(x) &= 2x T_m(x) - T_{m-1}(x), \end{aligned} \quad (10)$$

$$\begin{aligned} U_0(x) &= 1, & U_{-1}(x) &= 0, \\ U_{m+1}(x) &= 2x U_m(x) - U_{m-1}(x), \end{aligned} \quad (11)$$

which illustrate that Eqs. (8) and (9) indeed describe polynomials, and which, moreover, are an integral part of the iterative numerical scheme we develop later on. Two other useful relations are given by

$$2 T_m(x) T_n(x) = T_{m+n}(x) + T_{m-n}(x), \quad (12)$$

$$2(x^2 - 1) U_{m-1}(x) U_{n-1}(x) = T_{m+n}(x) - T_{m-n}(x), \quad (13)$$

and when calculating Green functions we also need Hilbert transforms of the polynomials,

$$\mathcal{P} \int_{-1}^1 \frac{T_n(y) dy}{(y-x)\sqrt{1-y^2}} = \pi U_{n-1}(x), \quad (14)$$

$$\mathcal{P} \int_{-1}^1 \frac{\sqrt{1-y^2} U_{n-1}(y) dy}{(y-x)} = -\pi T_n(x), \quad (15)$$

where \mathcal{P} denotes the principal value.

2. Modified moments

As sketched above, the standard way of expanding a function $f : [-1, 1] \rightarrow \mathbb{R}$ in terms of Chebyshev polynomials of first kind is given by

$$f(x) = \sum_{n=0}^{\infty} \frac{\langle f | T_n \rangle_1}{\langle T_n | T_n \rangle_1} T_n(x) = \alpha_0 + 2 \sum_{n=1}^{\infty} \alpha_n T_n(x) \quad (16)$$

with coefficients

$$\alpha_n = \langle f | T_n \rangle_1 = \int_{-1}^1 \frac{f(x) T_n(x)}{\pi\sqrt{1-x^2}} dx. \quad (17)$$

However, the calculation of these coefficients requires integrations over the weight function $w(x)$, which in practical applications to matrix problems prohibits a simple iterative scheme. The solution to this problem follows from a slight rearrangement of the expansion, namely

$$f(x) = \frac{1}{\pi\sqrt{1-x^2}} \left[\mu_0 + 2 \sum_{n=1}^{\infty} \mu_n T_n(x) \right] \quad (18)$$

with coefficients

$$\mu_n = \int_{-1}^1 f(x) T_n(x) dx. \quad (19)$$

More formally this rearrangement of the Chebyshev series corresponds to using the second scalar product $\langle \cdot | \cdot \rangle_2$ and expanding in terms of the orthogonal functions

$$\phi_n(x) = \frac{T_n(x)}{\pi\sqrt{1-x^2}}, \quad (20)$$

which fulfil the orthogonality relations

$$\langle \phi_n | \phi_m \rangle_2 = \frac{1+\delta_{n,0}}{2} \delta_{n,m}. \quad (21)$$

The expansion (18) is thus equivalent to

$$\begin{aligned} f(x) &= \sum_{n=0}^{\infty} \frac{\langle f | \phi_n \rangle_2}{\langle \phi_n | \phi_n \rangle_2} \phi_n(x) \\ &= \frac{1}{\pi\sqrt{1-x^2}} \left[\mu_0 + 2 \sum_{n=1}^{\infty} \mu_n T_n(x) \right] \end{aligned} \quad (22)$$

with moments

$$\mu_n = \langle f | \phi_n \rangle_2 = \int_{-1}^1 f(x) T_n(x) dx. \quad (23)$$

The μ_n now have the form of modified moments that we announced in the introduction, and Eqs. (18) and (19) represent the elementary basis for the numerical method which we review in this article. In the remaining sections we will explain how to translate physical quantities into polynomial expansions of the form (18), how to calculate the moments μ_n in practise, and, most importantly, how to regularise expansions of finite order.

Naturally, the moments μ_n depend on the considered quantity $f(x)$ and on the underlying model. We will specify these details when discussing particular applications in section III. Nevertheless, there are features which are similar to all types of applications, and we start with presenting these general aspects in what follows.

B. Calculation of moments

1. General considerations

A common feature of basically all Chebyshev expansions is the requirement for a rescaling of the underlying

matrix or Hamiltonian H . As we described above, the Chebyshev polynomials of both first and second kind are defined on the real interval $[-1, 1]$, whereas the quantities we are interested in usually depend on the eigenvalues $\{E_k\}$ of the considered (finite-dimensional) matrix. To fit this spectrum into the interval $[-1, 1]$ we apply a simple linear transformation to the Hamiltonian and all energy scales,

$$\tilde{H} = (H - b)/a, \quad (24)$$

$$\tilde{E} = (E - b)/a, \quad (25)$$

and denote all rescaled quantities with a tilde hereafter. Given the extremal eigenvalues of the Hamiltonian, E_{\min} and E_{\max} , which can be calculated, e.g. with the Lanczos algorithm [24], or for which bounds may be known analytically, the scaling factors a and b read

$$a = (E_{\max} - E_{\min})/(2 - \epsilon), \quad (26)$$

$$b = (E_{\max} + E_{\min})/2. \quad (27)$$

The parameter ϵ is a small cut-off introduced to avoid stability problems that arise if the spectrum includes or exceeds the boundaries of the interval $[-1, 1]$. It can be fixed, e.g. to $\epsilon = 0.01$, or adapted to the resolution of the calculation, which for an expansion of finite order N is proportional $1/N$ (see below).

The next similarity of most Chebyshev expansions is the form of the moments, namely their dependence on the matrix or Hamiltonian \tilde{H} . In general, we find two types of moments: Simple expectation values of Chebyshev polynomials in \tilde{H} ,

$$\mu_n = \langle \beta | T_n(\tilde{H}) | \alpha \rangle, \quad (28)$$

where $|\alpha\rangle$ and $|\beta\rangle$ are certain states of the system, or traces over such polynomials and a given operator A ,

$$\mu_n = \text{Tr}[A T_n(\tilde{H})]. \quad (29)$$

Handling the first case is rather straightforward. Starting from the state $|\alpha\rangle$ we can iteratively construct the states $|\alpha_n\rangle = T_n(\tilde{H})|\alpha\rangle$ by using the recursion relations for the T_n , Eq. (10),

$$|\alpha_0\rangle = |\alpha\rangle, \quad (30)$$

$$|\alpha_1\rangle = \tilde{H}|\alpha_0\rangle, \quad (31)$$

$$|\alpha_{n+1}\rangle = 2\tilde{H}|\alpha_n\rangle - |\alpha_{n-1}\rangle. \quad (32)$$

Scalar products with $|\beta\rangle$ then directly yield

$$\mu_n = \langle \beta | \alpha_n \rangle. \quad (33)$$

This iterative calculation of the moments, in particular the application of \tilde{H} to the state $|\alpha_n\rangle$, represents the most time consuming part of the whole expansion approach and determines its performance. If \tilde{H} is a sparse matrix of dimension D the matrix vector multiplication

is an order $O(D)$ process and the calculation of N moments therefore requires $O(ND)$ operations and time. The memory consumption depends on the implementation. For moderate problem dimension we can store the matrix and, in addition, need memory for two vectors of dimension D . For very large D the matrix certainly does not fit into memory and has to be reconstructed on-the-fly in each iteration or retrieved from disc. The two vectors then determine the memory consumption of the calculation. Overall, the resource consumption of the moment iteration is similar or even slightly better than that of the Lanczos algorithm, which requires a few more vector operations (see our comparison in section V). In contrast to Lanczos, the Chebyshev iteration is completely stable and can be carried out to arbitrary high order.

The moment iteration can be simplified even further, if $|\beta\rangle = |\alpha\rangle$. In this case the product relation (12) allows for the calculation of two moments from each new $|\alpha_n\rangle$,

$$\mu_{2n} = 2\langle\alpha_n|\alpha_n\rangle - \mu_0, \quad (34)$$

$$\mu_{2n+1} = 2\langle\alpha_{n+1}|\alpha_n\rangle - \mu_1, \quad (35)$$

which is equivalent to two moments per matrix vector multiplication. The numerical effort for N moments is thus reduced by a factor of two. In addition, like many other numerical approaches KPM benefits considerably from the use of symmetries that reduce the Hilbert space dimension.

2. Stochastic evaluation of traces

The second case where the moments depend on a trace over the whole Hilbert space, at first glance, looks far more complicated. Based on the previous considerations we would estimate the numerical effort to be proportional to D^2 , because the iteration needs to be repeated for all D states of a given basis. It turns out, however, that extremely good approximations of the moments can be obtained with a much simpler approach: the stochastic evaluation of the trace [13, 38, 39], i.e., an estimate of μ_n based on the average over only a small number $R \ll D$ of randomly chosen states $|r\rangle$,

$$\mu_n = \text{Tr}[A T_n(\tilde{H})] \approx \frac{1}{R} \sum_{r=0}^{R-1} \langle r | A T_n(\tilde{H}) | r \rangle. \quad (36)$$

The number of random states, R , does not scale with D . It can be kept constant or even reduced with increasing D . To understand this, let us consider the convergence properties of the above estimate. Given an arbitrary basis $\{|i\rangle\}$ and a set of independent identically distributed random variables $\xi_{ri} \in \mathbb{C}$, which in terms of the statistical average $\langle\langle \dots \rangle\rangle$ fulfil

$$\langle\langle \xi_{ri} \rangle\rangle = 0, \quad (37)$$

$$\langle\langle \xi_{ri} \xi_{r'j} \rangle\rangle = 0, \quad (38)$$

$$\langle\langle \xi_{ri}^* \xi_{r'j} \rangle\rangle = \delta_{rr'} \delta_{ij}, \quad (39)$$

a random vector is defined through

$$|r\rangle = \sum_{i=0}^{D-1} \xi_{ri} |i\rangle. \quad (40)$$

We can now calculate the statistical expectation value of the trace estimate $\Theta = \frac{1}{R} \sum_{r=0}^{R-1} \langle r | B | r \rangle$ for some Hermitian operator B with matrix elements $B_{ij} = \langle i | B | j \rangle$, and indeed find,

$$\begin{aligned} \langle\langle \Theta \rangle\rangle &= \langle\langle \frac{1}{R} \sum_{r=0}^{R-1} \langle r | B | r \rangle \rangle\rangle = \frac{1}{R} \sum_{r=0}^{R-1} \sum_{i,j=0}^{D-1} \langle\langle \xi_{ri}^* \xi_{rj} \rangle\rangle B_{ij} \\ &= \sum_{i=0}^{D-1} B_{ii} = \text{Tr}(B). \end{aligned} \quad (41)$$

Of course, this only shows that we obtain the correct result on average, and we therefore also need to study the fluctuation of Θ , which is characterised by $(\delta\Theta)^2 = \langle\langle \Theta^2 \rangle\rangle - \langle\langle \Theta \rangle\rangle^2$. Evaluating

$$\begin{aligned} \langle\langle \Theta^2 \rangle\rangle &= \langle\langle \frac{1}{R^2} \sum_{r,r'=0}^{R-1} \langle r | B | r \rangle \langle r' | B | r' \rangle \rangle\rangle \\ &= \frac{1}{R^2} \sum_{r,r'=0}^{R-1} \sum_{i,j,i',j'=0}^{D-1} \langle\langle \xi_{ri}^* \xi_{rj} \xi_{r'i'}^* \xi_{r'j'} \rangle\rangle B_{ij} B_{i'j'} \\ &= \frac{1}{R^2} \left(\sum_{r,r'=0}^{R-1} \sum_{\substack{i,j,i',j'=0 \\ r \neq r'}}^{D-1} \delta_{ij} \delta_{i'j'} B_{ij} B_{i'j'} \right. \\ &\quad \left. + \sum_{r=0}^{R-1} \sum_{i,j,i',j'=0}^{D-1} \langle\langle \xi_{ri}^* \xi_{rj} \xi_{ri'}^* \xi_{rj'} \rangle\rangle B_{ij} B_{i'j'} \right) \\ &= \frac{R-1}{R} (\text{Tr } B)^2 + \frac{1}{R} \left(\sum_{j=0}^{D-1} \langle\langle |\xi_{rj}|^4 \rangle\rangle B_{jj}^2 \right. \\ &\quad \left. + \sum_{\substack{i,j=0 \\ i \neq j}}^{D-1} B_{ii} B_{jj} + \sum_{\substack{i,j=0 \\ i \neq j}}^{D-1} B_{ij} B_{ji} \right) \\ &= (\text{Tr } B)^2 + \frac{1}{R} \left(\text{Tr}(B^2) + (\langle\langle |\xi_{ri}|^4 \rangle\rangle - 2) \sum_{j=0}^{D-1} B_{jj}^2 \right) \end{aligned} \quad (42)$$

we get for the fluctuation

$$(\delta\Theta)^2 = \frac{1}{R} \left(\text{Tr}(B^2) + (\langle\langle |\xi_{ri}|^4 \rangle\rangle - 2) \sum_{j=0}^{D-1} B_{jj}^2 \right). \quad (43)$$

The trace of B^2 will usually be of order $O(D)$, and the relative error of the trace estimate, $\delta\Theta/\Theta$, is thus of order $O(1/\sqrt{RD})$. It is this favourable behaviour, which ensures the convergence of the stochastic approach, and which was the basis for our initial statement that the number of random states $R \ll D$ can be kept small or even be reduced with the problem dimension D .

Note also that the distribution of the elements of $|r\rangle$, $p(\xi_{ri})$, has a slight influence on the precision of the estimate, since it determines the expectation value $\langle\langle |\xi_{ri}|^4 \rangle\rangle$ that enters Eq. (43). For an optimal distribution $\langle\langle |\xi_{ri}|^4 \rangle\rangle$ should be as close as possible to its lower bound $\langle\langle |\xi_{ri}|^2 \rangle\rangle^2 = 1$, and indeed, we find this result if we fix the amplitude of the ξ_{ri} and allow only for a random phase $\phi \in [0, 2\pi]$, $\xi_{ri} = e^{i\phi}$. Moreover, if we were working in the eigenbasis of B this would cause $\delta\Theta$ to vanish entirely, which led some authors [40] to conclude that random phase vectors are the optimal choice for stochastic trace estimates. However, all these considerations depend on the basis that we are working in, which in practice will never be the eigenbasis of B (in particular, if B corresponds to something like $A T_n(\tilde{H})$, as in Eq. (36)). A random phase vector in one basis does not necessarily correspond to a random phase vector in another basis, but the other basis may well lead to smaller value of $\sum_{j=0}^{D-1} B_{jj}^2$, thus compensating for the larger value of $\langle\langle |\xi_{ri}|^4 \rangle\rangle$. We therefore think that the actual choice of the distribution of ξ_{ri} is not of high practical significance, as long as Eqs. (37)–(39) for $\xi_{ri} \in \mathbb{C}$, or

$$\langle\langle \xi_{ri} \rangle\rangle = 0, \quad (44)$$

$$\langle\langle \xi_{ri} \xi_{r'j} \rangle\rangle = \delta_{rr'} \delta_{ij}, \quad (45)$$

for $\xi_{ri} \in \mathbb{R}$ are fulfilled. Typically we will consider Gaussian [13, 38] or uniformly distributed variables $\xi_{ri} \in \mathbb{R}$.

C. Kernel polynomials and Gibbs oscillations

1. Expansions of finite order & simple kernels

In the preceding sections we introduced the basic ideas underlying the expansion of a function $f(x)$ in an *infinite* series of Chebyshev polynomials, and gave a few hints for the numerical calculation of the expansion coefficients μ_n . As expected for a numerical approach, however, the total number of these moments will remain finite, and we thus arrive at a classical problem of approximation theory. Namely, we are looking for the best (uniform) approximation to $f(x)$ by a polynomial of given maximal degree, which in our case is equivalent to finding the best approximation to $f(x)$ given a *finite* number N of moments μ_n . To our advantage, such problems have been studied for at least 150 years and we can make use of results by many renowned mathematicians, such as Chebyshev, Weierstrass, Dirichlet, Fejér, Jackson, to name only a few.

Experience shows that a simple truncation of an infinite series,

$$f(x) \approx \frac{1}{\pi\sqrt{1-x^2}} \left[\mu_0 + 2 \sum_{n=1}^{N-1} \mu_n T_n(x) \right], \quad (46)$$

leads to poor precision and fluctuations (Gibbs oscillations) near discontinuities of the function $f(x)$, see Fig-

ure 1 below. A common procedure to damp these oscillations relies on an appropriate modification of the expansion coefficients, $\mu_n \rightarrow g_n \mu_n$, which changes with the order of the approximation,

$$\begin{aligned} f_{\text{KPM}}(x) &= \sum_{n=0}^{N-1} g_n \frac{\langle f | \phi_n \rangle_2}{\langle \phi_n | \phi_n \rangle_2} \phi_n(x) \\ &= \frac{1}{\pi\sqrt{1-x^2}} \left[g_0 \mu_0 + 2 \sum_{n=1}^{N-1} g_n \mu_n T_n(x) \right]. \end{aligned} \quad (47)$$

This truncation of the infinite series to order N together with the corresponding modification of the coefficients is equivalent to the convolution of $f(x)$ with a kernel of the form

$$K_N(x, y) = g_0 \phi_0(x) \phi_0(y) + 2 \sum_{n=1}^{N-1} g_n \phi_n(x) \phi_n(y), \quad (48)$$

namely

$$f_{\text{KPM}}(x) = \langle K_N(x, y) | f(y) \rangle_2. \quad (49)$$

The problem now translates into finding an optimal kernel $K_N(x, y)$, i.e., coefficients g_n , where the notion of “optimal” partially depends on the considered application.

The simplest kernel, which is usually attributed to Dirichlet, is obtained by setting $g_n^D = 1 \forall n \in [0, N-1]$,

$$K_N^D(x, y) = \phi_0(x) \phi_0(y) + 2 \sum_{n=1}^{N-1} \phi_n(x) \phi_n(y). \quad (50)$$

Obviously, convolution of $K_N^D(x, y)$ with a function $f(y)$ yields the above truncated series (46), whose disadvantages we mentioned briefly.

A first improvement is due to Fejér who showed that for continuous functions an approximation based on the kernel

$$K_N^F(x, y) = \frac{1}{N} \sum_{\nu=1}^N K_\nu^D(x, y), \quad \text{i.e., } g_n^F = 1 - \frac{n}{N}, \quad (51)$$

converges uniformly with an error of order $O(1/\sqrt{N})$. An essential condition for this convergence is the positivity of the kernel, $K_N^F(x, y) > 0 \forall x, y \in [-1, 1]$ [36, 37], which we can prove easily: Let us introduce the positive 2π -periodic function

$$p(\varphi) = \left| \sum_{\nu=0}^{N-1} a_\nu e^{i\nu\varphi} \right|^2 \quad (52)$$

with arbitrary $a_\nu \in \mathbb{R}$. Straight-forward calculation gives

$$\begin{aligned} p(\varphi) &= \sum_{\nu, \mu=0}^{N-1} a_\nu a_\mu e^{i(\nu-\mu)\varphi} = \sum_{\nu, \mu=0}^{N-1} a_\nu a_\mu \cos(\nu - \mu)\varphi \\ &= \sum_{\nu=0}^{N-1} a_\nu^2 + 2 \sum_{n=1}^{N-1} \sum_{\nu=0}^{N-1-n} a_\nu a_{\nu+n} \cos n\varphi. \end{aligned} \quad (53)$$

Hence, with

$$g_n = \sum_{\nu=0}^{N-1-n} a_\nu a_{\nu+n} \quad (54)$$

the function

$$p(\varphi) = g_0 + 2 \sum_{n=1}^{N-1} g_n \cos n\varphi \quad (55)$$

is positive and periodic in φ . However, if $p(\varphi)$ is positive, then the expression $\frac{1}{2}[p(\arccos x + \arccos y) + p(\arccos x - \arccos y)]$ is positive $\forall (x, y) \in [-1, 1]^2$. Using Eq. (8) and $\cos \alpha \cos \beta = \frac{1}{2}[\cos(\alpha + \beta) + \cos(\alpha - \beta)]$, we immediately observe that the general kernel $K_N(x, y)$ from Eq. (48) is positive $\forall (x, y) \in [-1, 1]^2$, if the coefficients g_n depend on arbitrary coefficients $a_\nu \in \mathbb{R}$ via Eq. (54). Setting $a_\nu = 1/\sqrt{N}$ yields the Fejér kernel $K_N^F(x, y)$, thus immediately proving its positivity.

2. Jackson kernel

In terms of its analytical properties and of the convergence of the approximation the Fejér kernel is a major improvement over the Dirichlet kernel. However, it does not sufficiently damp the unwanted Gibbs oscillations illustrated in Figure 1. Since so far we have not fully exhausted the freedom in choosing the coefficients a_ν , we can further improve the kernel, which will lead us to recover old results by Jackson [41, 42]. In particular, let us demand the following properties:

1. The kernel is positive.
2. The kernel is normalised in the sense that

$$\int_{-1}^1 f_{\text{KPM}}(x) dx = \int_{-1}^1 f(x) dx, \quad (56)$$

which is equivalent to $\langle \phi_0 | f_{\text{KPM}} \rangle_2 = \langle \phi_0 | f \rangle_2$.

3. The kernel has optimal resolution in the sense that

$$Q := \int_{-1}^1 \int_{-1}^1 (x - y)^2 K_N(x, y) dx dy \quad (57)$$

is minimal. Since $K_N(x, y)$ will be peaked at $x = y$, Q is basically the squared width of this peak.

The first condition, as mentioned before, makes the mapping $f \rightarrow f_{\text{KPM}}$ monotonic and ensures convergence of the approximation. The second condition is particularly useful for expansions of normalised quantities. Applying the kernel, for example, to a density of states thus yields an approximation which is strictly positive and

normalised, as we would expect. The third condition is, of course, the most important, since it puts our concept of an optimal approximation into equations. To fulfil all three requirements we proceed as follows:

1. The positivity we discussed already and found that it is guaranteed by choosing the g_n according to Eq. (54).
2. Our particular form of normalisation, Eq. (56), simply requires

$$g_0 = \sum_{\nu=0}^{N-1} a_\nu^2 \stackrel{!}{=} 1, \quad (58)$$

as can be seen, e.g. from Eq. (47). The Dirichlet and Fejér kernels therefore are normalised.

3. To express the variance Q of the kernel in terms of g_n and a_ν , respectively, note that

$$\begin{aligned} (x - y)^2 &= (T_1(x) - T_1(y))^2 \\ &= \frac{1}{2}(T_2(x) + T_0(x))T_0(y) - 2T_1(x)T_1(y) \\ &\quad + \frac{1}{2}T_0(x)(T_2(y) + T_0(y)). \end{aligned} \quad (59)$$

Using the orthogonality of the Chebyshev polynomials and inserting Eqs. (48) and (59) into (57), we can thus rephrase the condition of optimal resolution as

$$Q = g_0 - g_1 \stackrel{!}{=} \text{minimal w.r.t. } a_\nu. \quad (60)$$

Minimising $Q = g_0 - g_1$ under the constraint $C = g_0 - 1 = 0$ yields the condition

$$\frac{\partial Q}{\partial a_\nu} = \lambda \frac{\partial C}{\partial a_\nu}, \quad (61)$$

where λ is a Lagrange multiplier. Using Eq. (54) and setting $a_{-1} = a_N = 0$ we arrive at

$$2a_\nu - a_{\nu-1} - a_{\nu+1} = \lambda a_\nu \quad (62)$$

which the alert reader recognises as the eigenvalue problem of a harmonic chain with fixed boundary conditions. Its solution is given by

$$\begin{aligned} a_\nu &= \bar{a} \sin \frac{\pi k(\nu + 1)}{N + 1}, \\ \lambda &= 1 - \cos \frac{\pi k}{N + 1}, \end{aligned} \quad (63)$$

where $\nu = 0, \dots, (N - 1)$ and $k = 1, 2, \dots, N$. Given a_ν and the abbreviation $q = \pi k/(N + 1)$

we can easily calculate the g_n :

$$\begin{aligned}
g_n &= \sum_{\nu=0}^{N-1-n} a_\nu a_{\nu+n} = \bar{a}^2 \sum_{\nu=1}^{N-n} \sin q\nu \sin q(\nu+n) \\
&= \frac{\bar{a}^2}{2} \sum_{\nu=1}^{N-n} [\cos qn - \cos q(2\nu+n)] \\
&= \frac{\bar{a}^2}{2} \left[(N-n) \cos qn - \operatorname{Re} \sum_{\nu=1}^{N-n} e^{i q(2\nu+n)} \right] \\
&= \frac{\bar{a}^2}{2} [(N-n+1) \cos qn + \sin qn \cot q] .
\end{aligned} \tag{64}$$

The normalisation $g_0 = 1$ is ensured through $\bar{a}^2 = 2/(N+1)$, and with $g_1 = \cos q$ we can directly read off the optimal value for

$$Q = g_0 - g_1 = 1 - \cos \frac{\pi k}{N+1} , \tag{65}$$

which is obtained for $k = 1$,

$$Q_{\min} = 1 - \cos \frac{\pi}{N+1} \simeq \frac{1}{2} \left(\frac{\pi}{N} \right)^2 . \tag{66}$$

The latter result shows that for large N the resolution \sqrt{Q} of the new kernel is proportional to $1/N$. Clearly, this is an improvement over the Fejér kernel $K_N^F(x, y)$ which gives only $\sqrt{Q} = 1/\sqrt{N}$.

With the above calculation we reproduced results by Jackson [41, 42], who showed that with a similar kernel a continuous function can be approximated by a polynomial of degree $N-1$ with an error of the order of $O(1/N)$. Hereafter we are thus referring to the new optimal kernel as the Jackson kernel $K_N^J(x, y)$, with

$$g_n^J = \frac{(N-n+1) \cos \frac{\pi n}{N+1} + \sin \frac{\pi n}{N+1} \cot \frac{\pi}{N+1}}{N+1} . \tag{67}$$

The resolution $\sqrt{Q_{\min}}$ obtained in Eq. (66) is mainly a measure for the spread of the kernel $K_N^J(x, y)$ in the x - y -plane. However, for practical calculations it is often reasonable to ask for the broadening of a δ -function under convolution with the kernel,

$$\begin{aligned}
\delta_{\text{KPM}}(x-a) &= \langle K_N(x, y) | \delta(y-a) \rangle_2 \\
&= g_0 \phi_0(x) T_0(a) + 2 \sum_{n=1}^{N-1} g_n \phi_n(x) T_n(a) ,
\end{aligned} \tag{68}$$

which can be characterised by its variance $\sigma^2 = \langle x^2 \rangle - \langle x \rangle^2$. With $x = T_1(x)$ and $x^2 = [T_2(x) + T_0(x)]/2$ we find

$$\langle x \rangle = \int_{-1}^1 x \delta_{\text{KPM}}(x-a) dx = g_1 T_1(a) , \tag{69}$$

$$\begin{aligned}
\langle x^2 \rangle &= \int_{-1}^1 x^2 \delta_{\text{KPM}}(x-a) dx = \frac{g_0 T_0(a) + g_2 T_2(a)}{2} .
\end{aligned} \tag{70}$$

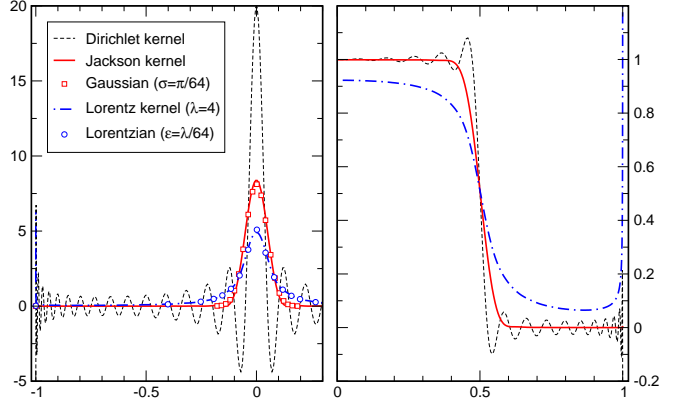


FIG. 1: Order $N = 64$ expansions of $\delta(x)$ (left) and a box function (right) based on different kernels. Whereas the truncated series (Dirichlet kernel) strongly oscillate, the Jackson results smoothly converge to the expanded functions. The Lorentz kernel leads to relatively poor convergence at the boundaries $x = \pm 1$, but otherwise yields perfect Lorentz-broadened approximations.

Hence, for $K_N^J(x, y)$ the squared width of $\delta_{\text{KPM}}(x-a)$ is given by

$$\begin{aligned}
\sigma^2 &= \langle x^2 \rangle - \langle x \rangle^2 = a^2 (g_2^J - (g_1^J)^2) + (g_0^J - g_2^J)/2 \\
&= \frac{N-a^2(N-1)}{2(N+1)} \left(1 - \cos \frac{2\pi}{N+1} \right) \\
&\simeq \left(\frac{\pi}{N} \right)^2 \left[1 - a^2 + \frac{3a^2-2}{N} \right] .
\end{aligned} \tag{71}$$

Using the Jackson kernel, an order N expansion of a δ -function at $x = 0$ thus results in a broadened peak of width $\sigma = \frac{\pi}{N}$, whereas close to the boundaries, $a = \pm 1$, we find $\sigma = \frac{\pi}{N^{3/2}}$. It turns out that this peak is a good approximation to a Gaussian,

$$\delta_{\text{KPM}}^J(x) \approx \frac{1}{\sqrt{2\pi\sigma^2}} \exp \left(-\frac{x^2}{2\sigma^2} \right) , \tag{72}$$

which we illustrate in Figure 1.

3. Lorentz kernel

The Jackson kernel derived in the preceding section is the best choice for most of the applications we discuss below. In some situations, however, special analytical properties of the expanded functions become important, which only other kernels can account for. The Green functions that appear in the Cluster Perturbation Theory, section IV B, are an example. Considering the imaginary part of the Plemelj-Dirac formula which frequently occurs in connexion with Green functions,

$$\lim_{\epsilon \rightarrow 0} \frac{1}{x + i\epsilon} = \mathcal{P} \left(\frac{1}{x} \right) - i\pi\delta(x) , \tag{73}$$

the δ -function on the right hand side is approached in terms of a Lorentz curve,

$$\delta(x) = -\frac{1}{\pi} \lim_{\epsilon \rightarrow 0} \text{Im} \frac{1}{x + i\epsilon} = \lim_{\epsilon \rightarrow 0} \frac{\epsilon}{\pi(x^2 + \epsilon^2)}, \quad (74)$$

which has a different and broader shape compared to the approximations of $\delta(x)$ we get with the Jackson kernel. Since we know that the Fourier transform of such a Lorentz peak is given by $\exp(-\epsilon|k|)$, we can try to construct an appropriate positive kernel assuming $a_\nu = e^{-\lambda\nu/N}$ in Eq. (54). After normalisation, $g_0 = 1$, this yields what we call the Lorentz kernel $K_N^L(x, y)$ hereafter,

$$g_n^L = \frac{\sinh[\lambda(1 - n/N)]}{\sinh(\lambda)}. \quad (75)$$

The variable λ is a free parameter of the kernel which as a compromise between good resolution and sufficient damping of the Gibbs oscillations we empirically choose to be of the order of 3...5. It is related to the ϵ -parameter of the Lorentz curve, i.e. to its resolution, via $\epsilon = \lambda/N$. Note also, that in the limit $\lambda \rightarrow 0$ we recover the Fejér kernel $K_N^F(x, y)$ with $g_n^F = 1 - n/N$.

In Figure 1 we compare truncated Chebyshev expansions — equivalent to using the Dirichlet kernel — to the approximations obtained with the Jackson and Lorentz kernels, which we will later use almost exclusively. Clearly, both kernels yield much better approximations to the expanded functions and, in particular, the wild oscillations have disappeared almost completely. The comparison with a Gaussian or Lorentzian, respectively, illustrates the nature of the broadening of a δ -function under convolution with the kernels, which later on will facilitate the interpretation of our numerical results. With Table I we conclude this section on kernels, and, for the sake of completeness, also list two other kernels that are occasionally used in the literature. Both have certain disadvantages, in particular, they are not strictly positive.

D. Implementational details and remarks

1. Discrete cosine & Fourier transforms

Having discussed the theory behind Chebyshev expansion, the calculation of moments, and the various kernel approximations, let us now come to the practical issues of the implementation of KPM. Assuming a finite number N of coefficients μ_n is known (see section III for details), the convolution with the kernel is equivalent to multiplying the μ_n with the factors g_n ,

$$\tilde{\mu}_n = \mu_n g_n. \quad (76)$$

We then usually want to reconstruct the expanded function $f(x)$ on a finite set of abscissas x_k , and naively we

could sum up Eq. (47) separately for each point, thereby making use of the recursion relations for T_n . We can do much better, however, by choosing our data points to be $x_k = \cos \varphi_k$ with

$$\varphi_k = \frac{\pi(k + 1/2)}{\tilde{N}} \quad \text{and} \quad k = 0, \dots, (\tilde{N} - 1), \quad (77)$$

which coincide with the abscissas of Chebyshev numerical integration [34]. The number \tilde{N} of points in the set $\{x_k\}$ is not necessarily the same as the number of moments N . Usually we will consider $\tilde{N} \geq N$ and a reasonable choice is, e.g. $\tilde{N} = 2N$. Due to the equidistant distribution of the angles φ_k the values $f(x_k)$ can now be obtained through discrete cosine transform,

$$\begin{aligned} \gamma_k &= \pi \sin \varphi_k f(\cos \varphi_k) \\ &= \tilde{\mu}_0 + 2 \sum_{n=1}^{\tilde{N}-1} \tilde{\mu}_n \cos \left(\frac{\pi n(k + 1/2)}{\tilde{N}} \right) \end{aligned} \quad (78)$$

which allows for the use of divide-and-conquer type algorithms that require only $\tilde{N} \log \tilde{N}$ operations. Corresponding routines are implemented in most Fast Fourier Transform (FFT) libraries, for instance, in FFTW [44] that ships with many Linux distributions.

If no implementation of the discrete cosine transform is at hand we may also use fast discrete Fourier transform. With

$$\lambda_n = \begin{cases} (2 - \delta_{n,0}) \tilde{\mu}_n \exp\left(\frac{i\pi n}{2N}\right) & 0 < n < N \\ 0 & \text{otherwise} \end{cases} \quad (79)$$

and the standard definition of discrete Fourier transform,

$$\tilde{\lambda}_k = \sum_{n=0}^{\tilde{N}-1} \lambda_n \exp\left(\frac{2\pi i n k}{\tilde{N}}\right), \quad (80)$$

after some reordering we find for an even number of data points

$$\gamma_{2j} = \text{Re}(\tilde{\lambda}_j), \quad (81)$$

$$\gamma_{2j+1} = \text{Re}(\tilde{\lambda}_{\tilde{N}-1-j}), \quad (82)$$

with $j = 0, \dots, \tilde{N}/2 - 1$. If we need only a discrete cosine transform this setup is not optimal, as it makes no use of the imaginary part which the complex FFT calculates. It turns out, however, that the “lost” imaginary part is exactly what we need when we later calculate Green functions and other complex quantities, i.e., we can use the setup

$$\tilde{\gamma}_{2j} = \tilde{\lambda}_j, \quad (83)$$

$$\tilde{\gamma}_{2j+1} = \tilde{\lambda}_{\tilde{N}-1-j}^*, \quad (84)$$

to evaluate Eq. (120).

Name	g_n	Parameters	positive?	Remarks
Jackson	$\frac{1}{N+1}[(N-n+1)\cos\frac{\pi n}{N+1} + \sin\frac{\pi n}{N+1}\cot\frac{\pi}{N+1}]$	none	yes	best for most applications
Lorentz	$\sinh[\lambda(1-n/N)]/\sinh(\lambda)$	λ	yes	best for Green functions
Fejér	$1-n/N$	none	yes	mainly of academic interest
Lanczos	$\left(\frac{\sin(\pi n/N)}{\pi n/N}\right)^M$	$M \in \mathbb{N}$	no	$M = 3$ closely matches the Jackson kernel, but not strictly positive [43]
Wang and Zunger	$\exp[-(\alpha\frac{n}{N})^\beta]$	α, β	no	found empirically, not optimal [14, 15]
Dirichlet	1	none	no	least favourable choice

TABLE I: Summary of the different integral kernels that can be used to achieve convergence of an order N Chebyshev series. The coefficients g_n refer to Eq. (47) or (48), respectively.

2. Integrals involving expanded functions

We have already mentioned that our particular choice of x_k corresponds to the abscissas of numerical Chebyshev integration. Hence, Gauss-type numerical approximations to integrals of the form $\int_{-1}^1 f(x)g(x)dx$ become simple sums,

$$\begin{aligned} \int_{-1}^1 f(x)g(x)dx &= \int_{-1}^1 \frac{\sqrt{1-x^2}f(x)g(x)}{\sqrt{1-x^2}}dx \\ &\simeq \frac{\pi}{\tilde{N}} \sum_{k=0}^{\tilde{N}-1} \sqrt{1-x_k^2} f(x_k)g(x_k) = \frac{1}{\tilde{N}} \sum_{k=0}^{\tilde{N}-1} \gamma_k g(x_k), \end{aligned} \quad (85)$$

where γ_k denotes the raw output of the cosine or Fourier transforms defined in Eq. (78). We can use this feature, for instance, to calculate partition functions, where $f(x)$ corresponds to the expansion of the spectral density $\rho(E)$ and $g(x)$ to the Boltzmann or Fermi weight.

E. Generalisation to higher dimension

1. Expansion of multivariate functions

For the calculation of finite-temperature dynamical correlation functions we will later need expansions of functions of two variables. Let us therefore comment on the generalisation of the previous considerations to d -dimensional space, which is easily obtained by extending the scalar product $\langle \cdot | \cdot \rangle_2$ to functions $f, g : [-1, 1]^d \rightarrow \mathbb{R}$,

$$\langle f | g \rangle_2 = \int_{-1}^1 \cdots \int_{-1}^1 f(\vec{x})g(\vec{x}) \left(\prod_{j=1}^d \pi \sqrt{1-x_j^2} \right) dx_1 \dots dx_d. \quad (86)$$

Here x_j denote the d components of the vector \vec{x} . Naturally, this scalar product leads to the expansion

$$\begin{aligned} f(\vec{x}) &= \sum_{\vec{n}=\vec{0}}^{\infty} \frac{\langle f | \phi_{\vec{n}} \rangle_2}{\langle \phi_{\vec{n}} | \phi_{\vec{n}} \rangle_2} \phi_{\vec{n}}(\vec{x}) \\ &= \frac{\sum_{\vec{n}=\vec{0}}^{\infty} \mu_{\vec{n}} w_{\vec{n}} \prod_{j=1}^d T_{n_j}(x_j)}{\prod_{j=1}^d \pi \sqrt{1-x_j^2}}, \end{aligned} \quad (87)$$

where we introduced a vector notation for indices, $\vec{n} = \{n_1, \dots, n_d\}$, and the following functions and coefficients

$$\phi_{\vec{n}}(\vec{x}) = \prod_{j=1}^d \phi_{n_j}(x_j), \quad (88)$$

$$\begin{aligned} \mu_{\vec{n}} &= \langle f | \phi_{\vec{n}} \rangle_2 \\ &= \int_{-1}^1 \cdots \int_{-1}^1 f(\vec{x}) \left(\prod_{j=1}^d T_{n_j}(x_j) \right) dx_1 \dots dx_d, \end{aligned} \quad (89)$$

$$w_{\vec{n}} = \frac{1}{\langle \phi_{\vec{n}} | \phi_{\vec{n}} \rangle_2} = \prod_{j=1}^d \frac{2}{1 + \delta_{n_j, 0}}. \quad (90)$$

2. Kernels for finite order expansions

As in the one-dimensional case, a simple truncation of the infinite series will lead to Gibbs oscillations and poor convergence. Fortunately, we can easily generalise our previous results for kernel approximations. In particular, we find that the extended kernel

$$K_N(\vec{x}, \vec{y}) = \prod_{j=1}^d K_N(x_j, y_j) \quad (91)$$

maps an infinite series onto an truncated series,

$$\begin{aligned} f_{\text{KPM}}(\vec{x}) &= \langle K_N(\vec{x}, \vec{y}) | f(\vec{y}) \rangle_2 \\ &= \frac{\sum_{\vec{n}=\vec{0}}^{N-1} \mu_{\vec{n}} w_{\vec{n}} \prod_{j=1}^d g_{n_j} T_{n_j}(x_j)}{\prod_{j=1}^d \pi \sqrt{1-x_j^2}}, \end{aligned} \quad (92)$$

where we can take the g_n of any of the previously discussed kernels. If we use the g_n^J of the Jackson kernel, $K_N^J(\vec{x}, \vec{y})$ fulfils generalisations of our conditions for an optimal kernel, namely

1. $K_N^J(\vec{x}, \vec{y})$ is positive $\forall \vec{x}, \vec{y} \in [-1, 1]^d$.

2. $K_N^J(\vec{x}, \vec{y})$ is normalised with

$$\int_{-1}^1 \cdots \int_{-1}^1 f_{\text{KPM}}(\vec{x}) dx_1 \dots dx_d = \int_{-1}^1 \cdots \int_{-1}^1 f(\vec{x}) dx_1 \dots dx_d. \quad (93)$$

3. $K_N^J(\vec{x}, \vec{y})$ has optimal resolution in the sense that

$$\begin{aligned} Q &= \int_{-1}^1 \cdots \int_{-1}^1 (\vec{x} - \vec{y})^2 K_N(\vec{x}, \vec{y}) dx_1 \dots dx_d dy_1 \dots dy_d \\ &= d(g_0 - g_1) \end{aligned} \quad (94)$$

is minimal.

Note that for simplicity the order of the expansion, N , was chosen to be the same for all spatial directions. Of course, we could also define more general kernels,

$$K_{\vec{N}}(\vec{x}, \vec{y}) = \prod_{j=1}^d K_{N_j}(x_j, y_j), \quad (95)$$

where the vector \vec{N} denotes the orders of expansion for the different spatial directions.

3. Reconstruction with cosine transforms

Similar to the 1D case we may consider the function $f : [-1, 1]^d \rightarrow \mathbb{R}$ on a discrete grid $\vec{x}_{\vec{k}}$ with

$$x_{\vec{k},j} = \cos(\varphi_{k_j}), \quad (96)$$

$$\varphi_{k_j} = \frac{\pi(k_j + 1/2)}{\tilde{N}}, \quad (97)$$

$$k_j = 0, \dots, (\tilde{N} - 1). \quad (98)$$

Note again that we could define individual numbers of points for each spatial direction, i.e., a vector $\vec{\tilde{N}}$ with elements \tilde{N}_j instead of a single \tilde{N} . For all grid points $\vec{x}_{\vec{k}}$ the function $f(\vec{x}_{\vec{k}})$ is obtained through multidimensional discrete cosine transform, i.e., with coefficients $\kappa_{\vec{n}} = \tilde{\mu}_{\vec{n}} w_{\vec{n}} = \mu_{\vec{n}} g_{\vec{n}} w_{\vec{n}}$ we find

$$\begin{aligned} \gamma_{\vec{k}} &= f(\cos(\varphi_{k_1}), \dots, \cos(\varphi_{k_d})) \prod_{j=1}^d \pi \sin(\varphi_{k_j}) \\ &= \sum_{\vec{n}=\vec{0}}^{N-1} \kappa_{\vec{n}} \prod_{j=1}^d \cos(n_j \varphi_{k_j}) \\ &= \sum_{n_1=0}^{N-1} \cos(n_1 \varphi_{k_1}) \dots \sum_{n_d=0}^{N-1} \cos(n_d \varphi_{k_d}) \kappa_{\vec{n}} \end{aligned} \quad (99)$$

The last line shows that the multidimensional discrete cosine transform is equivalent to a nesting of one-dimensional transforms in every coordinate. With fast implementations the computational effort is thus proportional to $d\tilde{N}^{d-1}\tilde{N} \log \tilde{N}$, which equals the expected value for \tilde{N}^d data points, $\tilde{N}^d \log \tilde{N}^d$. If we are not using libraries like FFTW, which provide ready-to-use multidimensional routines, we may also resort to one-dimensional cosine transform or the above translation into FFT to obtain high-performance implementations of general d -dimensional transforms.

III. APPLICATIONS OF KPM

Having described the mathematical background and many details of the implementation of the Kernel Polynomial Method (KPM), we are now in the position to present practical applications of the approach. Already in the introduction we have mentioned that KPM can be used whenever we are interested in the spectral properties of large matrices or in correlation functions that can be expressed through the eigenstates of such matrices. Apparently, this leads to a vast range of applications. In what follows, we try to cover all types of accessible quantities and for each give at least one example. We thereby focus on lattice models from solid state physics.

A. Densities of states

1. General considerations

The first and basic application of Chebyshev expansion and KPM is the calculation of the spectral densities of Hermitian matrices, which could correspond to the densities of states of both interacting or non-interacting quantum models [7, 13, 16, 38]. For the beginning, let us consider a model of non-interacting fermions $c_i^{(\dagger)}$, described by the Hamiltonian

$$H = \sum_{i,j} c_i^\dagger M_{ij} c_j. \quad (100)$$

Here M is an arbitrary Hermitian matrix of dimension D , and knowing the spectrum of M , i.e., the single particle density of states $\rho(E)$, all thermodynamic quantities can be calculated. For example, the particle density is given by

$$n = \int \frac{\rho(E)}{1 + e^{\beta(E-\mu)}} dE \quad (101)$$

and the free energy per site reads

$$f = n\mu - \frac{1}{\beta} \int \rho(E) \log(1 + e^{-\beta(E-\mu)}) dE, \quad (102)$$

where μ is the chemical potential and $\beta = (k_B T)^{-1}$ the inverse temperature.

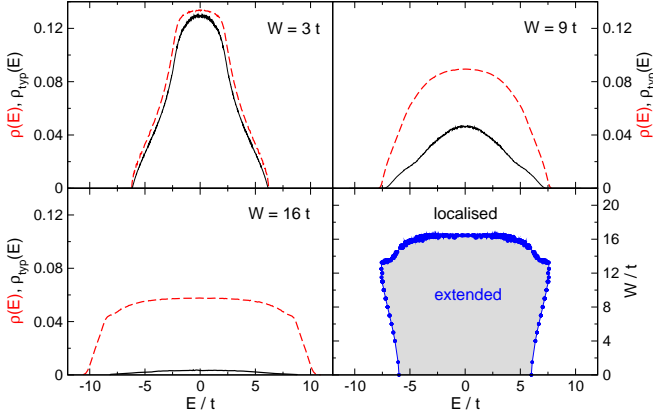


FIG. 2: Standard and typical density of states, $\rho(E)$ and $\rho_{\text{typ}}(E)$ respectively, of the 3D Anderson model on a 50^3 site cluster with periodic boundary conditions. For $\rho(E)$ we calculated $N = 2048$ moments with $R = 10$ start vectors and $S = 240$ realisations of disorder, for $\rho_{\text{typ}}(E)$ these numbers are $N = 8192$, $R = 32$ and $S = 200$. The lower right panel shows the phase diagram of the model we obtained from $\rho_{\text{typ}}(E)/\rho(E) \rightarrow 0$ (mobility edge).

As described earlier, the expansion of $\rho(E)$ in terms of Chebyshev polynomials requires a rescaling of $M \rightarrow \tilde{M}$, such that the spectrum of $\tilde{M} = (M - b)/a$ lies within the interval $[-1, 1]$. Given the eigenvalues \tilde{E}_k of \tilde{M} the rescaled density of states $\tilde{\rho}(E)$ reads

$$\tilde{\rho}(E) = \frac{1}{D} \sum_{k=0}^{D-1} \delta(E - \tilde{E}_k), \quad (103)$$

and according to Equation (19) the expansion coefficients become

$$\begin{aligned} \mu_n &= \int_{-1}^1 \tilde{\rho}(E) T_n(E) dE = \frac{1}{D} \sum_{k=0}^{D-1} T_n(\tilde{E}_k) \\ &= \frac{1}{D} \sum_{k=0}^{D-1} \langle k | T_n(\tilde{M}) | k \rangle = \frac{1}{D} \text{Tr}(T_n(\tilde{M})). \end{aligned} \quad (104)$$

This is exactly the trace form that we introduced in section II B, and we can immediately calculate the μ_n using the stochastic techniques described in section II B 2. Knowing the moments we can use the techniques of section II D to reconstruct $\rho(E)$ for the whole range of energies.

2. Non-interacting systems: Anderson model of disorder

As the first physical example let us consider the Anderson model of non-interacting fermions moving in a random potential [45],

$$H = -t \sum_{\langle ij \rangle} c_i^\dagger c_j + \sum_i \epsilon_i c_i^\dagger c_i. \quad (105)$$

Here hopping occurs along nearest neighbour bonds $\langle ij \rangle$ on a simple cubic lattice and the local potential ϵ_i is chosen randomly with uniform distribution in the interval $[-W/2, W/2]$. With increasing strength of disorder, W , the single particle eigenstates of the model tend to become localised in the vicinity of a particular lattice site, which excludes these states from contributing to electronic transport. Disorder can therefore drive a transition from metallic behaviour with delocalised fermions to insulating behaviour with localised fermions [46, 47, 48]. The disorder averaged density of states $\rho(E)$ of the model can be obtained as described, but it contains no information about the metal-insulator transition. The KPM method, however, allows also for the calculation of the local density of states,

$$\rho_i(E) = \frac{1}{D} \sum_{k=0}^{D-1} |\langle i | k \rangle|^2 \delta(E - E_k), \quad (106)$$

which is a measure for the contribution of a single lattice site (denoted by the basis state $|i\rangle$) to the complete spectrum. For delocalised states all sites contribute equally, whereas localised states reside on just a few sites, or, equivalently, a certain site contributes only to a few eigenstates. This property has a pronounced effect on the distribution of $\rho_i(E)$, which at a fixed energy E characterises the variation of ρ_i over different realisations of disorder and sites i . For energies that correspond localised eigenstates the distribution is highly asymmetric and becomes singular in the thermodynamic limit, whereas in the delocalised case the distribution is regular and centred near its expectation value $\rho(E)$. Therefore a comparison of the geometric and the arithmetic average of $\rho_i(E)$ over a set of realisations of disorder and over lattice sites reveals the position of the Anderson transition [49, 50, 51]. The expansion of $\rho_i(E)$ is even simpler than the expansion of $\rho(E)$, since the moments have the form of expectation values and do not involve a trace,

$$\begin{aligned} \mu_n &= \int_{-1}^1 \tilde{\rho}_i(E) T_n(E) dE = \frac{1}{D} \sum_{k=0}^{D-1} |\langle i | k \rangle|^2 T_n(\tilde{E}_k) \\ &= \frac{1}{D} \sum_{k=0}^{D-1} \langle i | T_n(\tilde{M}) | k \rangle \langle k | i \rangle = \frac{1}{D} \langle i | T_n(\tilde{M}) | i \rangle. \end{aligned} \quad (107)$$

In Figure 2 we show the standard density of states $\rho(E)$, which coincides with the arithmetic mean of $\rho_i(E)$, in comparison to the so called typical density of states $\rho_{\text{typ}}(E)$, which is defined as the geometric mean of $\rho_i(E)$,

$$\rho_{\text{typ}}(E) = \exp[\langle\langle \log(\rho_i(E)) \rangle\rangle]. \quad (108)$$

With increasing disorder, starting from the boundaries of the spectrum, $\rho_{\text{typ}}(E)$ is suppressed until it vanishes completely for $W \gtrsim 16.5$, which is known as the critical strength of disorder where the states in the band centre become localised [52]. The calculation yields the

phase diagram shown in the lower right corner of Figure 2, which compares well to other numerical results.

Since the method requires storage only for the sparse Hamiltonian matrix and for two vectors of the corresponding dimension, quite large systems can be studied on standard desktop computers (of the order of 100^3 sites). The recursion is stable for arbitrarily high expansion order. In the present case we calculated as many as 8192 moments to achieve maximum resolution in the local density of states. The standard DOS is usually far less demanding.

3. Interacting systems: Double exchange

Coming to interacting quantum systems, as a second example we study the evolution of the quantum double exchange model [53] for large spin amplitude S , which in terms of spin-less fermions $c_i^{(\dagger)}$ and Schwinger bosons $a_{i\sigma}^{(\dagger)}$ ($\sigma = \uparrow, \downarrow$) is given by the Hamiltonian

$$H = -\frac{t}{2S+1} \sum_{\langle ij \rangle, \sigma} a_{i\sigma}^\dagger a_{j\sigma} c_i^\dagger c_j \quad (109)$$

with the local constraint $\sum_\sigma a_{i\sigma}^\dagger a_{i\sigma} = 2S + c_i^\dagger c_i$. This model describes itinerant electrons on a lattice whose spin is strongly coupled to local spins of amplitude S , so that the motion of the electrons mediates an effective ferromagnetic interaction between these localised spins. In the case of colossal magneto-resistant manganites [54], for instance, cubic site symmetry leads to a crystal field splitting of the manganese d -shell, and three electrons in the resulting t_{2g} -shell form the local spins. The remaining electrons occupy the e_g -shell and can become itinerant upon doping, causing these materials to show ferromagnetic order [55]. If the ferromagnetic (Hund's rule) coupling is large, at each site only the high-spin states are relevant and we can describe the total on-site spin in terms of Schwinger bosons $a_{i\sigma}^{(\dagger)}$ [56]. From the electrons only the charge degree of freedom remains, which is denoted by the spin-less fermions $c_i^{(\dagger)}$ (see, e.g. [57] for more details). The full quantum model (109) is rather complicated for analytical or numerical studies, and we expect major simplification by treating the spin background classically (remember that S is quite large for the systems of interest). The limit of classical spins, $S \rightarrow \infty$, is obtained by averaging Eq. (109) over spin coherent states,

$$|\Omega(S, \theta, \phi)\rangle = \frac{(\cos(\frac{\theta}{2}) e^{i\phi/2} a_\uparrow^\dagger + \sin(\frac{\theta}{2}) e^{-i\phi/2} a_\downarrow^\dagger)^{2S}}{\sqrt{(2S)!}} |0\rangle, \quad (110)$$

where θ and ϕ are the classical polar angles and $|0\rangle$ the bosonic vacuum. The resulting non-interacting Hamiltonian reads,

$$H = -\sum_{\langle ij \rangle} t_{ij} c_i^\dagger c_j + \text{H.c.}, \quad (111)$$

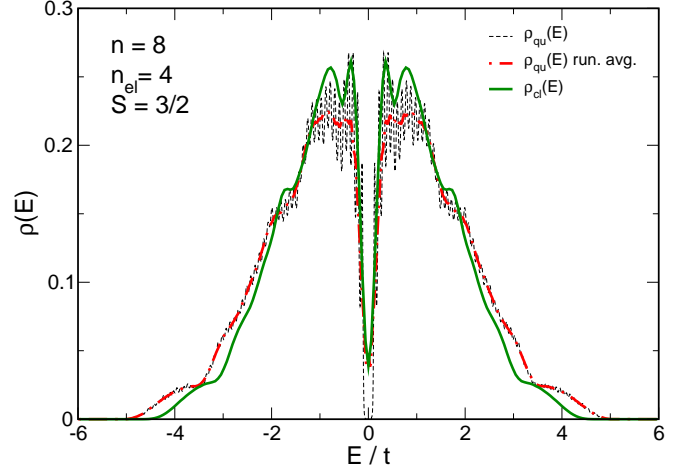


FIG. 3: Density of nonzero eigenvalues of the quantum double-exchange model with $S = 3/2$ (dashed line) and running average (red dot-dashed), calculated for 4 electrons on a 8-site ring, compared to the classical result $S \rightarrow \infty$ (green solid). Expansion parameters: $N = 400$ moments and $R = 100$ random vectors per S^z sector.

with the matrix element [58]

$$t_{ij} = t \left[\cos \frac{\theta_i}{2} \cos \frac{\theta_j}{2} e^{-i(\phi_i - \phi_j)/2} + \sin \frac{\theta_i}{2} \sin \frac{\theta_j}{2} e^{i(\phi_i - \phi_j)/2} \right], \quad (112)$$

i.e., spin-less fermions move in a background of random or ordered classical spins which affect their hopping amplitude.

To assess the quality of this classical approximation we considered four electrons moving on a ring of eight sites, and compared the densities of states obtained for a background of $S = 3/2$ quantum spins and a background of classical spins. For the full quantum Hamiltonian, Eq. (109), the (canonical) density of states was calculated on the basis of 400 Chebyshev moments. To reduce the Hilbert space dimension and to save resources, in addition, we made use of the $SU(2)$ symmetry of the model: With the stochastic approach we calculated separate moments $\mu_n^{S^z}$ for each S^z -sector,

$$\mu_n^{S^z} = \text{Tr}^{S^z} [T_n(\tilde{H})], \quad (113)$$

and used the dimensions D^{S^z} of the sectors to obtain the total normalised μ_n from the average

$$\mu_n = \frac{1}{D} \text{Tr}[T_n(\tilde{H})] = \frac{\sum_{S^z=-S^{\max}}^{S^{\max}} \mu_n^{S^z}}{\sum_{S^z=-S^{\max}}^{S^{\max}} D^{S^z}}. \quad (114)$$

Note, that such a setup can be used whenever the model under consideration has certain symmetries.

On the other hand, we solved the effective non-interacting model (111) and calculated the distributions

of non-zero energies for a background of fully disordered classical spins. As Figure 3 illustrates, the spectrum of the quantum model with $S = 3/2$ closely matches that of the system with classical spins, providing good justification, e.g. for studies of colossal magneto-resistive manganites that make use of a classical approximation for the spin background. Since for the finite cluster considered the spectrum of the quantum model is discrete, at the present expansion order KPM starts to resolve distinct energy levels (dashed line). Therefore a running average (dot-dashed line) compares better to the classical spin-averaged data (bold line).

B. Dynamical correlation functions at $T = 0$

1. General considerations

Densities of states provide only the most basic information about a given quantum system, and much more details can usually be learned from the response of the system to an external probe or perturbation. In the framework of linear response theory and the Kubo formalism this response is expressed in terms of dynamical correlation functions, which are the subject of this section. For an interacting quantum system at $T = 0$ a dynamical correlation function for two operators A and B can be defined through

$$\begin{aligned} \langle A; B \rangle_\omega &= \lim_{\epsilon \rightarrow 0} \langle 0 | A \frac{1}{\omega + i\epsilon - H} B | 0 \rangle \\ &= \lim_{\epsilon \rightarrow 0} \sum_{k=0}^{D-1} \frac{\langle 0 | A | k \rangle \langle k | B | 0 \rangle}{\omega + i\epsilon - E_k}, \end{aligned} \quad (115)$$

where E_k is the energy of the eigenstate $|k\rangle$ of the Hamiltonian, $|0\rangle$ the ground-state, and $\epsilon > 0$.

If we assume that the product $\langle 0 | A | k \rangle \langle k | B | 0 \rangle$ is real the imaginary part

$$\text{Im} \langle A; B \rangle_\omega = -\pi \sum_{k=0}^{D-1} \langle 0 | A | k \rangle \langle k | B | 0 \rangle \delta(\omega - E_k) \quad (116)$$

has a similar structure as the local density of states, Eq. (106). Hence, after rescaling the Hamiltonian $H \rightarrow \tilde{H}$ and all energies $\omega \rightarrow \tilde{\omega}$ it can be expanded in Chebyshev polynomials,

$$\text{Im} \langle A; B \rangle_{\tilde{\omega}} = -\frac{1}{\sqrt{1 - \tilde{\omega}^2}} \left[\mu_0 + 2 \sum_{n=1}^{\infty} \mu_n T_n(\tilde{\omega}) \right], \quad (117)$$

and the moments are obtained from expectation values

$$\mu_n = \frac{1}{\pi} \int_{-1}^1 \text{Im} \langle A; B \rangle_{\tilde{\omega}} T_n(\tilde{\omega}) d\tilde{\omega} = \langle 0 | A T_n(\tilde{H}) B | 0 \rangle. \quad (118)$$

Note that for $A \neq B^\dagger$ we can follow the scheme of Eqs. (30) to (33), whereas for $A = B^\dagger$ the calculation simplifies to the one in Eqs. (34) and (35) with $B|0\rangle$ as the starting vector.

In many cases, especially for the spectral functions and optical conductivities studied below, only the imaginary part of $\langle A; B \rangle_\omega$ is of interest. Sometimes however (e.g. within the Cluster Perturbation Theory; cf. Sec. IV B) also the real part is required. Fortunately it can be calculated with almost no additional effort: The analytical properties of $\langle A; B \rangle_\omega$ arising from causality imply that its real part is fully determined by the imaginary part. Indeed a Hilbert transform gives

$$\begin{aligned} \text{Re} \langle A; B \rangle_{\tilde{\omega}} &= \sum_{k=0}^{D-1} \langle 0 | A | k \rangle \langle k | B | 0 \rangle \mathcal{P} \left(\frac{1}{\tilde{\omega} - \tilde{E}_k} \right) \\ &= -\frac{1}{\pi} \mathcal{P} \int_{-1}^1 \frac{\text{Im} \langle A; B \rangle_{\tilde{\omega}'} d\tilde{\omega}'}{\tilde{\omega} - \tilde{\omega}'} = -2 \sum_{n=1}^{\infty} \mu_n U_{n-1}(\tilde{\omega}) \end{aligned} \quad (119)$$

where we used Eq. (14). The full correlation function

$$\begin{aligned} \langle A; B \rangle_{\tilde{\omega}} &= \frac{-i\mu_0}{\sqrt{1 - \tilde{\omega}^2}} - 2 \sum_{n=1}^{\infty} \mu_n \left[U_{n-1}(\tilde{\omega}) + \frac{i T_n(\tilde{\omega})}{\sqrt{1 - \tilde{\omega}^2}} \right] \\ &= \frac{-i}{\sqrt{1 - \tilde{\omega}^2}} \left[\mu_0 + 2 \sum_{n=1}^{\infty} \mu_n \exp(-i n \arccos \tilde{\omega}) \right] \end{aligned} \quad (120)$$

can thus be reconstructed from the same moments μ_n that we derived for its imaginary part, Eq. (118). In contrast to the real quantities we considered so far, the reconstruction merely requires complex Fourier transform, see Eqs. (83) and (84). If only the imaginary or real part of $\langle A; B \rangle_\omega$ is needed, a cosine or sine transform, respectively, is sufficient.

Note, that the calculation of dynamical correlation functions for non-interacting electron systems is *not* possible with the scheme discussed in this section, not even at zero temperature. At finite band filling the ground-state consists of a sum over occupied single-electron states, and dynamical correlation functions thus involve a double summation over matrix elements between all single-particle eigenstates, weighted by the Fermi function. Clearly, this is more complicated than (115), and we postpone the discussion of this case to section III D, where we describe methods for dynamical correlation functions at finite temperature and – for the case of non-interacting electrons – finite density.

2. One-particle spectral function

An important example of a dynamical correlation function is the (retarded) Green function in momentum space,

$$G_\sigma(\vec{k}, \omega) = \langle c_{\vec{k}, \sigma}; c_{\vec{k}, \sigma}^\dagger \rangle_\omega - \langle c_{\vec{k}, \sigma}^\dagger; c_{\vec{k}, \sigma} \rangle_{-\omega}, \quad (121)$$

and the associated spectral function

$$A_\sigma(\vec{k}, \omega) = -\frac{1}{\pi} \text{Im} G_\sigma(\vec{k}, \omega) = A_\sigma^+(\vec{k}, \omega) + A_\sigma^-(\vec{k}, \omega), \quad (122)$$

which characterises the electron absorption or emission of the interacting system. For instance, A_σ^- can be measured in angle resolved photo-emission spectroscopy (ARPES).

As an example, let us consider the one-dimensional Holstein Hubbard model,

$$H = -t \sum_{i,\sigma} (c_{i,\sigma}^\dagger c_{i+1,\sigma} + \text{H.c.}) + U \sum_i n_{i\uparrow} n_{i\downarrow} - g\omega_0 \sum_{i,\sigma} (b_i^\dagger + b_i) n_{i\sigma} + \omega_0 \sum_i b_i^\dagger b_i, \quad (123)$$

which describes a band of interacting electrons $c_{i\sigma}^{(\dagger)}$ that are coupled to the optical phonon modes $b_i^{(\dagger)}$ of the surrounding lattice. For low carrier density the model accounts for the formation of polarons, i.e., of heavy quasi particles consisting of an electron and an accompanying lattice distortion. At half band-filling the model allows for the study of the competition between two insulating phases, a Peierls (band) and a Mott (correlated) insulator.

Since the Hamiltonian (123) involves bosonic degrees of freedom, the Hilbert space of a finite system has infinite dimension. In practice, however, the contribution of highly excited phonon states is negligible at low temperature or for the ground-state, and the system is well approximated by a truncated phonon space with $\sum_i b_i^\dagger b_i \leq M$ [59]. In addition, the translational symmetry of the model can be used to reduce the Hilbert space dimension, and, moreover, the symmetric phonon mode with momentum $q = 0$ can be excluded from the numerics: Since it couples to the total number of electrons, which is a conserved quantity, its contribution can be handled analytically [60, 61]. For the present case, where the cluster size is $L = 8$ or 10 , a cut-off $M = 24$ or 15 , respectively, therefore results in truncation errors $< 10^{-6}$ for the ground-state energy.

Starting with the case of a single electron on a ten-site ring, Figure 4 (a) illustrates the presence of a polaron band at the Fermi level. To compare with available quantum MC data [62] we focus on the case where spin projection σ of the spectral function equals that of the electron on the ring, which makes the problem equivalent to that of spinless fermions. The excitations to or from the polaron band are given by the highest or lowest peaks of

$$A_\sigma^-(k, \omega) = \sum_l |\langle l, N_e - 1, S^z - \sigma | c_{k,\sigma} | 0, N_e, S^z \rangle|^2 \times \delta[\omega + (E_{l,N_e-1,S^z-\sigma} - E_{0,N_e,S^z})] \quad (124)$$

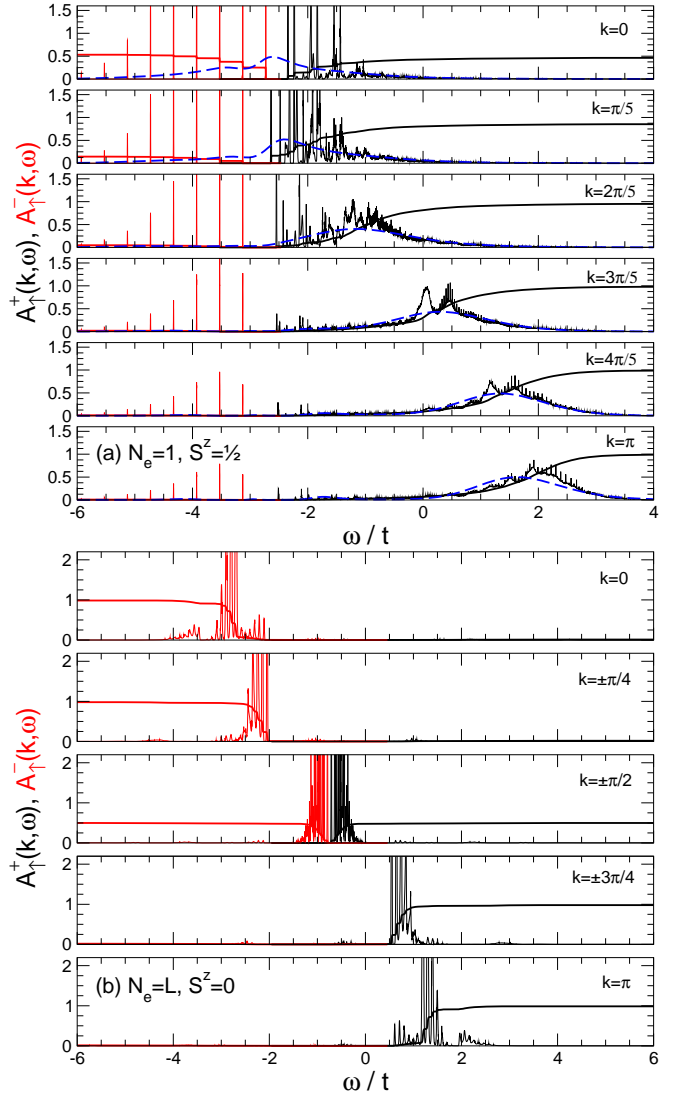


FIG. 4: One-particle spectral function and its integral for the Holstein Hubbard model (a) on a 10-site ring with one electron, $\varepsilon_p = g^2\omega_0 = 2.0t$, $\omega_0 = 0.4t$, and (b) on a 8-site ring, band filling $n = 0.5$, $\varepsilon_p = g^2\omega_0 = 0.7t$, $\omega_0 = 0.1t$, $U/t = 1.3$. For comparison, in (a) blue dashed curves represent Quantum Monte Carlo data at $\beta t = 8$ [62].

or

$$A_\sigma^+(k, \omega) = \sum_l |\langle l, N_e + 1, S^z + \sigma | c_{k,\sigma}^\dagger | 0, N_e, S^z \rangle|^2 \times \delta[\omega - (E_{l,N_e+1,S^z+\sigma} - E_{0,N_e,S^z})], \quad (125)$$

respectively, where $|l, N_e, S^z\rangle$ denotes the l th eigenstate with N_e electrons, spin projection S^z , and energy E_{l,N_e,S^z} . The photo-emission part A_σ^- reflects the Poisson-like phonon distribution of the one-electron ground state. The integrated spectral weight gives a measure for the electronic weight of the various poles in the one-electron spectrum. For example, it reveals that the phonon peaks in A_σ^- have very little weight. In fact,

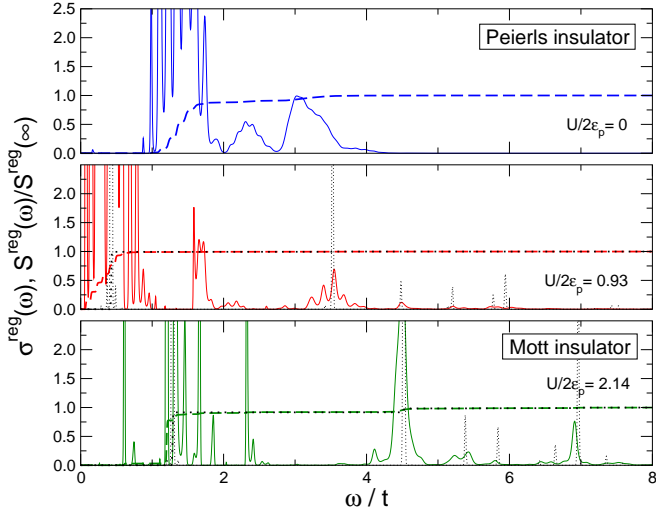


FIG. 5: The optical conductivity $\sigma^{\text{reg}}(\omega)$ and its integral $S^{\text{reg}}(\omega)$ for the Holstein Hubbard model at half-filling with different ratios of the Coulomb interaction U to the electron-lattice coupling $\epsilon_p = g^2\omega_0$, $\omega_0 = 0.1t$, and $g^2 = 7$. Black dotted lines denote excitations of the pure Hubbard model. The system size is $L = 8$.

the integrated weight jumps to a finite value at the first peaks near the Fermi level for $k = 0$ and $k = \pi/5$, while it changes very little as one moves further down in energy. For $k > \pi/5$, the small spectral weight contained in A_σ^- is continuously distributed among the phonon peaks. We also observe the well-known flattening of the polaron band at large values of k . The low-energy states have mostly electronic character at small k , and become mostly phononic at large values of k .

At half-filling, as a function of the Coulomb interaction U or the electron-lattice coupling g , the model shows a transition from a band (or Peierls) insulator to a Mott (or correlated) insulator, and the optical and charge gaps close at the transition point (see Refs. 63, 64 for more details). Figure 4 (b) shows the one-particle spectral function near this transition for an eight-site system with periodic boundary conditions. The largest matrix dimensions in the present examples were of the order of 10^8 to 10^{10} , which, of course, requires high-performance computers such as Hitachi SR8000-F1 or IBM p690 for the moment calculation. For the reconstruction of the spectra a desktop computer is nevertheless sufficient.

3. Optical conductivity

In the optical conductivity the imaginary and real parts of our general correlation functions $\langle A; B \rangle_\omega$ change their roles due to an additional frequency integration. The so-called regular contribution to the real part of the

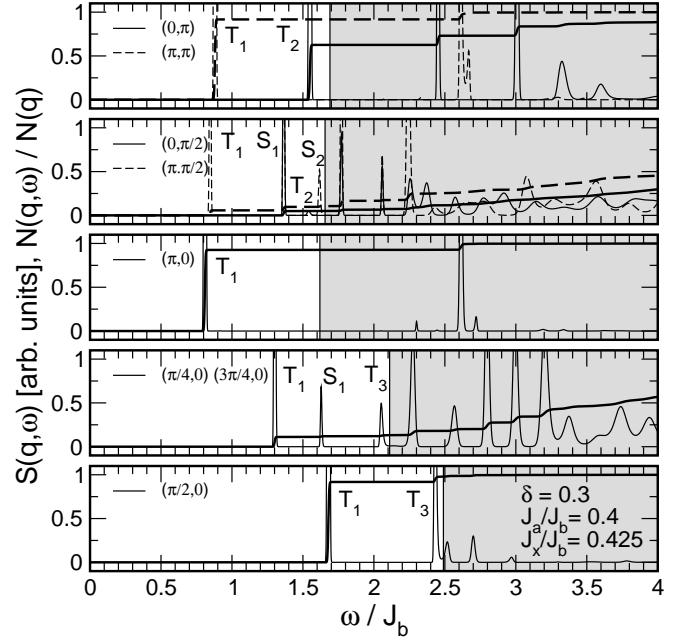


FIG. 6: Spin structure factor at $T = 0$ calculated for the model (128) which aims at describing the magnetic compound $(\text{VO})_2\text{P}_2\text{O}_7$. For more details see [65].

optical conductivity is thus given by,

$$\sigma^{\text{reg}}(\omega) = \frac{1}{\omega} \sum_{E_k > E_0} |\langle k | J | 0 \rangle|^2 \delta(\omega - (E_k - E_0)), \quad (126)$$

where the operator

$$J = -i \int q t \sum_{i, \sigma} (c_{i, \sigma}^\dagger c_{i+1, \sigma} - \text{H.c.}) \quad (127)$$

describes the current. After rescaling the energy and shifting the frequency, $\omega = \tilde{\omega} + \tilde{E}_0$, the sum can be expanded as described earlier, now with $J|0\rangle$ as the initial state. Back-scaling and dividing by ω then yields the final result. In Figure 5 we show the optical conductivity of the Holstein Hubbard model, which nicely complements the information obtained from the one-particle spectral function. The data clearly reflects the closing and re-opening of the optical gap with increasing Coulomb interaction, which we mentioned before. The system size is again eight sites and we used a phonon cut-off of $\sum_i b_i^\dagger b_i \leq 24$.

4. Spin structure factor

Apart from electron systems, of course, the KPM approach works also for other quantum problems such as pure spin systems. To describe the excitation spectrum and the magnetic properties of the compound $(\text{VO})_2\text{P}_2\text{O}_7$, some years ago we proposed the 2D spin

Hamiltonian [65]

$$H = J_b \sum_{i,j} (1 + \delta(-1)^i) \vec{S}_{i,j} \cdot \vec{S}_{i+1,j} + J_a \sum_{i,j} \vec{S}_{i,j} \cdot \vec{S}_{i,j+1} + J_x \sum_{i,j} (\vec{S}_{2i,j} \cdot \vec{S}_{2i+1,j+1} + \vec{S}_{2i+1,j} \cdot \vec{S}_{2i,j+1}), \quad (128)$$

where $\vec{S}_{i,j}$ denote spin-1/2 operators on a square lattice. With this model we aimed at explaining the observation of two branches of low-lying triplet excitations by neutron scattering [66], which was inconsistent with the then prevailing picture of $(\text{VO})_2\text{P}_2\text{O}_7$ being a spin-ladder or alternating chain compound.

Studying the low-energy physics of the model (128) the KPM approach can be used to calculate the spin structure factor and the integrated spectral weight,

$$S(\vec{q}, \omega) = \sum_k |\langle k | \vec{S}^z(\vec{q}) | 0 \rangle|^2 \delta(E_k - E_0 - \omega), \quad (129)$$

$$N(\vec{q}, \omega) = \int_0^\omega d\omega' S(\vec{q}, \omega'), \quad (130)$$

where $\vec{S}^z(\vec{q}) = \sum_{i,j} e^{i\vec{q} \cdot \vec{r}_{i,j}} S_{i,j}^z$. Figure 6 shows these quantities for a 4×8 cluster with periodic boundary conditions. The dimension of the sector $S_z = 0$, which contains the ground state, is rather moderate here being of the order of $D \approx 4 \cdot 10^7$ only. The expansion clearly resolves the lowest (massive) triplet excitations T_1 , a number of singlets and, in particular, a second triplet branch T_2 . The shaded region marks the two-particle continuum obtained by exciting two of the elementary triplets T_1 , and illustrates that T_2 is lower in energy.

C. Static correlations at $T > 0$

All the correlation functions considered so far characterise quantum systems in their ground state, i.e., at zero temperature. Starting with static correlation functions, let us now extend the application range of the expansion techniques to finite temperature. Given the eigenstates $|k\rangle$ of an interacting quantum system the thermodynamic expectation value of an operator A reads

$$\langle A \rangle = \frac{1}{ZD} \text{Tr}(A e^{-\beta H}) = \frac{1}{ZD} \sum_{k=0}^{D-1} \langle k | A | k \rangle e^{-\beta E_k}, \quad (131)$$

$$Z = \frac{1}{D} \text{Tr}(e^{-\beta H}) = \frac{1}{D} \sum_{k=0}^{D-1} e^{-\beta E_k}, \quad (132)$$

where H is the Hamiltonian of the system, Z the partition function, and E_k the energy of the eigenstate $|k\rangle$. Using the function

$$a(E) = \frac{1}{D} \sum_{k=0}^{D-1} \langle k | A | k \rangle \delta(E - E_k) \quad (133)$$

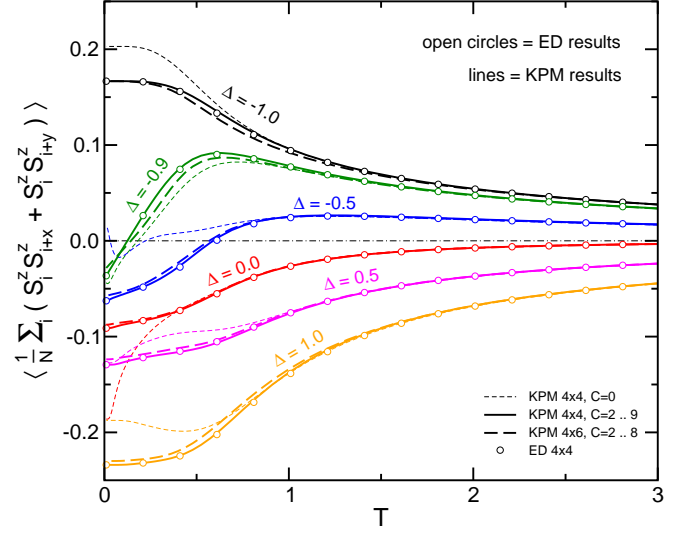


FIG. 7: Nearest-neighbour S^z - S^z correlations of the XXZ model on a 4×4 square lattice. Lines represent the KPM results with (bold solid) and without (thin dashed) separating low-lying eigenstates, open symbols denote exact results from a complete diagonalisation.

and the (canonical) density of states $\rho(E)$, we can express the thermal expectation value in terms of integrals over the Boltzmann weight,

$$\langle A \rangle = \frac{1}{Z} \int_{-\infty}^{\infty} a(E) e^{-\beta E} dE, \quad (134)$$

$$Z = \int_{-\infty}^{\infty} \rho(E) e^{-\beta E} dE. \quad (135)$$

Of course, similar relations hold also for non-interacting fermion systems, where the Boltzmann weight $e^{-\beta E}$ has to be replaced by the Fermi function $f(E) = (1 + e^{-\beta(E-\mu)})^{-1}$ and the single-electron wave functions play the role of $|k\rangle$.

Again, the particular form of $a(E)$ suggests an expansion in Chebyshev polynomials, and after rescaling we find

$$\begin{aligned} \mu_n &= \int_{-1}^1 \tilde{a}(E) T_n(E) dE = \frac{1}{D} \sum_{k=0}^{D-1} \langle k | A | k \rangle T_n(\tilde{E}_k) \\ &= \frac{1}{D} \text{Tr}(AT_n(\tilde{H})), \end{aligned} \quad (136)$$

which can be evaluated with the stochastic approach, section II B 2.

For interacting systems at low temperature the expression (134) is a bit problematic, since the Boltzmann factor puts most of the weight on the lower end of the spectrum and heavily amplifies small numerical errors in $\rho(E)$ and $a(E)$. We can avoid these problems by separating the

ground state and some of the lowest excitations from the rest of the spectrum, writing

$$\langle A \rangle = \frac{1}{ZD} \sum_{k=0}^{C-1} \langle k|A|k \rangle e^{-\beta E_k} + \frac{1}{Z} \int_{-\infty}^{\infty} a_s(E) e^{-\beta E} dE, \quad (137)$$

$$Z = \frac{1}{D} \sum_{k=0}^{C-1} e^{-\beta E_k} + \int_{-\infty}^{\infty} \rho_s(E) e^{-\beta E} dE \quad (138)$$

for the expectation value of A and the partition function Z . The functions

$$a_s(E) = \frac{1}{D} \sum_{k=C}^{D-1} \langle k|A|k \rangle \delta(E - E_k), \quad (139)$$

$$\rho_s(E) = \frac{1}{D} \sum_{k=C}^{D-1} \delta(E - E_k) \quad (140)$$

describe the rest of the spectrum and can be easily expanded in Chebyshev polynomials. Introducing the projection operator

$$P = 1 - \sum_{k=0}^{C-1} |k\rangle\langle k|, \quad (141)$$

we find for the expansion coefficients of $\tilde{a}_s(E)$

$$\mu_n = \frac{1}{D} \text{Tr}(PAT_n(\tilde{H})) \approx \frac{1}{RD} \sum_{r=0}^{R-1} \langle r|PAT_n(\tilde{H})P|r \rangle. \quad (142)$$

and similarly for those of $\tilde{\rho}_s(E)$

$$\mu_n = \frac{1}{D} \text{Tr}(PT_n(\tilde{H})) \approx \frac{1}{RD} \sum_{r=0}^{R-1} \langle r|PT_n(\tilde{H})P|r \rangle, \quad (143)$$

The eigenstates occurring in the projection P are obtained by standard exact diagonalisation methods like Lanczos or Jacobi-Davidson, and may require some amount of additional storage.

We illustrate the accuracy of this approach in Figure 7 considering the nearest-neighbour S^z - S^z correlations of the square-lattice spin-1/2 XXZ model as an example,

$$H = \sum_{i,\delta} (S_i^x S_{i+\delta}^x + S_i^y S_{i+\delta}^y + \Delta S_i^z S_{i+\delta}^z). \quad (144)$$

As a function of temperature and for an anisotropy $-1 < \Delta < 0$ this model shows a quantum to classical crossover in the sense that the correlations are anti-ferromagnetic at low temperature (quantum effect) and ferromagnetic at high temperature (as expected for the classical model). [67, 68, 69] Comparing the KPM results with the exact correlations of a 4×4 system, which were obtained from a complete diagonalisation of the Hamiltonian, the improvement due to the separation of only a few

low-lying eigenstates is obvious. Whereas for $C = 0$ the data is more or less random below $T \approx 1$, the agreement with the exact data is perfect, if the ground state and one or two excitations are considered separately. The numerical effort required for these calculations differs largely between complete diagonalisation and the KPM method. For the former, 18 or 20 sites are practically the limit, whereas the latter can easily handle 30 sites or more.

Note that for non-interacting systems the above separation of the spectrum is not required, since for $T \rightarrow 0$ the Fermi function converges to a simple step function without causing any numerical problems.

D. Dynamical correlations at finite temperature

1. General considerations

In section III B we mentioned briefly that for non-interacting electron systems the calculation of dynamical correlation functions is more involved, due to the required double summation over all matrix elements of the measured operators. The same holds for interacting systems as soon as we work at finite temperature. Chebyshev expansion, nevertheless, offers an efficient way for handling these problems. To be specific, let us derive all new ideas on the basis of the optical conductivity $\sigma(\omega)$, which will be our primary application below. Generalisations to other dynamical correlations can be derived without much effort.

For an interacting system the extension of Eq. (126) is given by

$$\sigma^{\text{reg}}(\omega) = \sum_{k,q} \frac{|\langle k|J|q \rangle|^2 (e^{-\beta E_k} - e^{-\beta E_q})}{ZD\omega} \delta(\omega - \omega_{qk}), \quad (145)$$

with $\omega_{qk} = E_q - E_k$ and Z the partition function. Compared to Eq. (126) a straight-forward expansion of the finite temperature conductivity is spoiled by the presence of the Boltzmann weighting factors. Some authors [31] try to handle this problem by expanding these factors in Chebyshev polynomials and performing a numerical time evolution subsequently, which, however, requires a new simulation for each temperature. A much simpler approach is based on the function

$$j(x, y) = \frac{1}{D} \sum_{k,q} |\langle k|J|q \rangle|^2 \delta(x - E_k) \delta(y - E_q) \quad (146)$$

which we may interpret as a matrix element density. Being a function of two variables, $j(x, y)$ can be expanded with two-dimensional KPM,

$$\tilde{j}(x, y) = \sum_{n,m=0}^{N-1} \frac{\mu_{nm} w_{nm} g_n g_m T_n(x) T_m(y)}{\pi^2 \sqrt{(1-x^2)(1-y^2)}} \quad (147)$$

where $\tilde{j}(x, y)$ refers to the rescaled $j(x, y)$, g_n are the usual kernel damping factors (see Eq. (67)), and w_{nm}

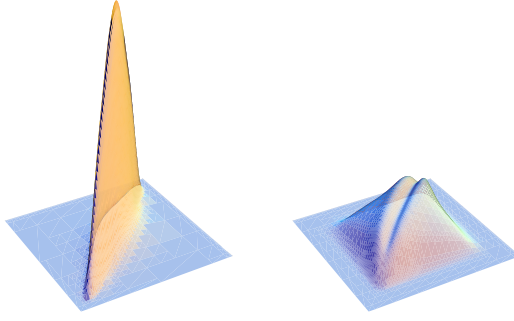


FIG. 8: The matrix element density $j(x, y)$ for the 3D Anderson model with disorder $W = 2$ and $W = 12$.

account for the correct normalisation (see Eq. (90)). The moments μ_{nm} are obtained from

$$\begin{aligned} \mu_{nm} &= \int_{-1}^1 \int_{-1}^1 \tilde{j}(x, y) T_n(x) T_m(y) dx dy \\ &= \frac{1}{D} \sum_{k,q} |\langle k | J | q \rangle|^2 T_n(\tilde{E}_k) T_m(\tilde{E}_q) \\ &= \frac{1}{D} \sum_{k,q} \langle k | T_n(\tilde{H}) J | q \rangle \langle q | T_m(\tilde{H}) J | k \rangle \\ &= \frac{1}{D} \text{Tr} (T_n(\tilde{H}) J T_m(\tilde{H}) J), \end{aligned} \quad (148)$$

and the trace can again be replaced by an average over a relatively small number R of random vectors $|r\rangle$. The numerical effort for an expansion of order $n, m < N$ ranges between $2RDN$ and RDN^2 , depending on whether memory is available for up to N vectors of the Hilbert space dimension D or not. Given the operator density $j(x, y)$ we find the optical conductivity by integration,

$$\begin{aligned} \sigma^{\text{reg}}(\omega) &= \frac{1}{Z\omega} \int_{-\infty}^{\infty} j(y + \omega, y) (e^{-\beta y} - e^{-\beta(y+\omega)}) dy \\ &= \sum_{k,q} \frac{|\langle k | J | q \rangle|^2 (e^{-\beta E_k} - e^{-\beta E_q})}{ZD\omega} \delta(\omega - \omega_{qk}), \end{aligned} \quad (149)$$

and, as above, we get the partition function Z by integrating over the density of states $\rho(E)$, which can be expanded in parallel to $j(x, y)$. Note that the calculation of the conductivity at different temperatures is based on the same operator density $j(x, y)$, i.e., it needs to be expanded only once for all temperatures.

Surprisingly, the basic steps of this approach were suggested already ten years ago [14, 15], but – probably overlooking its potential – applied only to the zero-temperature response of non-interacting electrons. A reason for the poor appreciation of these old ideas may also lie in the use of non-optimal kernels, which did not ensure the positivity of $j(x, y)$ and reduced the numerical precision. Only recently, one of the authors generalised the

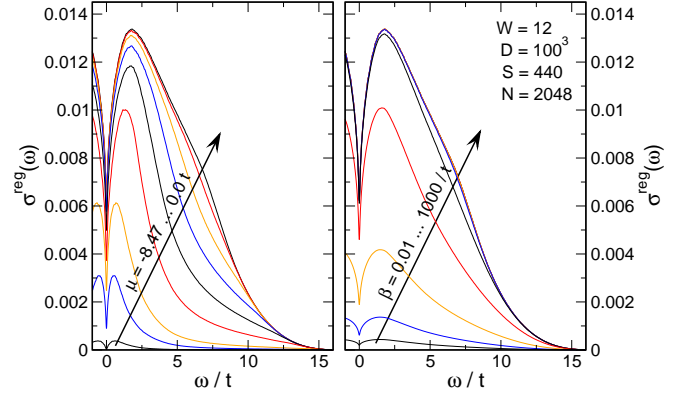


FIG. 9: Optical conductivity of the 3D Anderson model at disorder $W = 12$ and for different chemical potentials μ and temperatures $\beta = (kT)^{-1}$.

Jackson kernel and obtained high resolution optical data for the Anderson model [17]. More results, in particular for interacting quantum systems at finite temperature, we present hereafter.

2. Optical conductivity of the Anderson model

Since the Anderson model describes non-interacting fermions, the eigenstates $|k\rangle$ occurring in $\sigma(\omega)$ now denote single particle wave-functions and the Boltzmann weight has to be replaced by the Fermi function,

$$\begin{aligned} \sigma^{\text{reg}}(\omega) &= \frac{1}{\omega} \int_{-\infty}^{\infty} j(y + \omega, y) (f(y) - f(y + \omega)) dy \\ &= \sum_{k,q} \frac{|\langle k | J | q \rangle|^2 (f(E_k) - f(E_q))}{\omega} \delta(\omega - \omega_{qk}). \end{aligned} \quad (150)$$

Clearly, from a computational point of view this expression is of the same complexity for both, zero and finite temperature, and indeed, compared to section III B, we need the more advanced 2D KPM approach.

Figure 8 shows the matrix element density $j(x, y)$ calculated for the 3D Anderson model on a $D = 50^3$ site cluster. The expansion order is $N = 64$, and the moment data was averaged over $S = 10$ disorder samples and $R = 10$ random start vectors each. Starting from a “shark fin” at weak disorder, with increasing W the density $j(x, y)$ spreads in the entire energy plane, simultaneously developing a sharp dip along $x = y$. A comparison with Eq. (150) reveals that this dip is responsible for the decreasing and finally vanishing DC conductivity of the model [17]. In Figure 9 we show the resulting optical conductivity at $W = 12$ for different chemical potentials μ and temperatures $\beta = (kT)^{-1}$. Note that all curves are derived from the same matrix element density $j(x, y)$, which is now based on a $D = 100^3$ site cluster, expansion order $N = 2048$, an average over $S = 440$ samples and

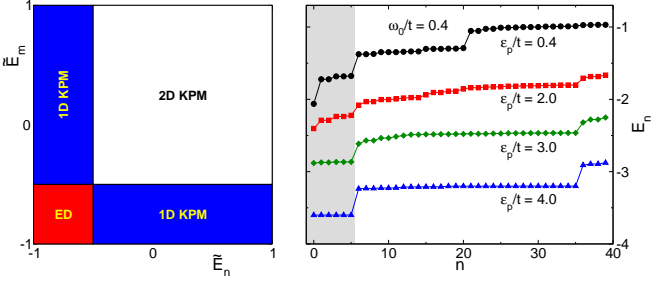


FIG. 10: Left: Schematic setup for the calculation of finite-temperature dynamical correlations for interacting quantum systems, which requires a separation into parts handled by exact diagonalisation (ED), 1D Chebyshev expansion and 2D Chebyshev expansion. Right: The lowest eigenvalues of the Holstein model on a six site chain for different electron-phonon coupling ϵ_p . The shaded region marks the lowest polaron band, which was handled separately when calculating the spectra in Figure 11.

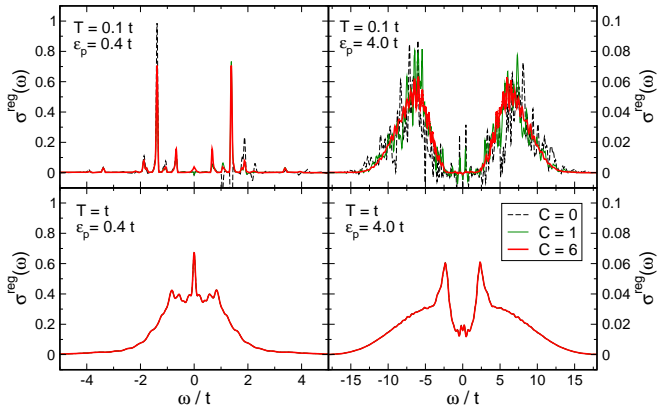


FIG. 11: Finite temperature optical conductivity of a single electron coupled to the lattice via a Holstein type interaction. Different colours illustrate how, in particular, the low-temperature spectra benefit from a separation of $C = 0, 1$ or 6 low-energy states [70].

only $R = 1$ random start vectors each.

3. Optical conductivity of the Holstein model

Having discussed dynamical correlations for non-interacting electrons, let us now come back to the case of interacting systems. The setup described so far works well for high temperatures, but as soon as T gets small we experience the same problems as with thermal expectation values. Again, the Boltzmann factors put most of the weight to the margins of the domain of $j(x, y)$, thus amplifying small numerical errors. To properly approach the limit $T \rightarrow 0$ we therefore have to separate the ground state and a few lowest excitations from the rest of the spectrum in a fashion similar to the static

correlations in section III C. Since we start from a 2D expansion, the correlation function (optical conductivity) now splits into three parts: a contribution from the transitions (or matrix elements) between the separated eigenstates, a sum of 1D expansions for the transitions between the separated states and the rest of the spectrum (see section III B), and a 2D expansion for all transitions within the rest of the spectrum,

$$\sigma^{\text{reg}}(\omega) = \underbrace{\sum_{k,q=0}^{C-1} \sigma_{k,q}}_{\sigma_{\text{ED}}^{\text{reg}}(\omega)} + \underbrace{\sum_{k=0}^{C-1} \sum_{q=C}^{D-1} (\sigma_{k,q} + \sigma_{q,k})}_{\sigma_{\text{1D}}^{\text{reg}}(\omega)} + \underbrace{\sum_{k,q=C}^{D-1} \sigma_{k,q}}_{\sigma_{\text{2D}}^{\text{reg}}(\omega)}, \quad (151)$$

with

$$\sigma_{k,q} = \frac{|\langle k | J | q \rangle|^2 (e^{-\beta E_k} - e^{-\beta E_q}) \delta(\omega - \omega_{qk})}{Z D \omega}. \quad (152)$$

The expansions required for $\sigma_{\text{1D}}^{\text{reg}}(\omega)$ are carried out in analogy to section III B 3, but the resulting conductivities are weighted appropriately when all contributions are combined to $\sigma^{\text{reg}}(\omega)$. Using the projection operator defined in Eq. (141), the corresponding moments read

$$\mu_n^k = \langle k | J P T_n(\tilde{H}) P J | k \rangle. \quad (153)$$

For $\sigma_{\text{2D}}^{\text{reg}}(\omega)$ we follow the scheme outlined in III D 1, but use projected moments

$$\mu_{nm} = \text{Tr}(T_n(\tilde{H}) P J T_m(\tilde{H}) P J) / D. \quad (154)$$

In Figure 10 we illustrate our setup schematically and show the lowest forty eigenvalues of the Holstein model with a band filling of one electron. Separating up to six states from the rest of the spectrum we obtain the finite-temperature optical conductivity of the system, Figure 11. For high temperatures ($T = t$, see lower panels) the separation of low-energy states is not necessary, the conductivity curves for $C = 0, 1$ and 6 agree very well. For low temperatures ($T = 0.1t$, see upper panels), the separation is crucial. Without any separated states ($C = 0$) the conductivity has substantial numerical errors and can even become negative, if large Boltzmann factors amplify infinitesimal numerical round-off errors of negative sign. Splitting off the ground state ($C = 1$) or the entire (narrow) polaron band ($C = 6$ for the present six-site cluster), we obtain reliable, high-resolution spectra down to the lowest temperatures. From a physics point of view, at strong electron phonon coupling (right panels) the conductivity shows an interesting transfer of spectral weight from high to low frequencies, if the temperature is increased (see Ref. [70] for more details).

With this discussion of optical conductivity as a finite temperature dynamical correlation function we conclude the section on direct applications of KPM. Of course, the described techniques can be used for the solution of many other interesting and numerically demanding problems, but an equally important field of applications emerges, when KPM is embedded into other numerical or analytical techniques, which is the subject of the next section.

IV. KPM AS A COMPONENT OF OTHER METHODS

A. Monte Carlo simulations

In condensed matter physics some of the most intensely studied materials are affected by a complex interplay of many degrees of freedom, and when deriving suitable approximate descriptions we frequently arrive at models, where non-interacting fermions are coupled to classical degrees of freedom. Examples are colossal magnetoresistant manganites or magnetic semiconductors, where the classical variables correspond to localised spin degrees of freedom. We already introduced such a model when we discussed the limit $S \rightarrow \infty$ of the double-exchange model, Eq. (111). The properties of these systems, e.g. a ferromagnetic ordering as a function of temperature, can be studied by standard MC procedures. However, in contrast to purely classical systems the energy of a given spin configuration, which enters the transition probabilities, cannot be calculated directly, but requires the solution of the corresponding non-interacting fermion problem. This is usually the most time consuming part, and an efficient MC algorithm should therefore evaluate the fermionic trace as fast and as seldom as possible.

The first requirement can be matched by using KPM for calculating the density of states of the fermion system, which by integration over the Fermi function yields the energy of the underlying spin configuration. Combined with standard Metropolis single-spin updates this led to the first MC simulations of double-exchange systems [71, 72, 73] on reasonably large clusters (8^3 sites), which were later improved by replacing full traces by trace estimates and by increasing the efficiency of the matrix vector multiplications [74, 75].

To fulfil the second requirement it would be advantageous to replace the above single-spin updates by updates of the whole spin background. The first implementation of such ideas was given in terms of an Hybrid Monte Carlo algorithm [76], which combines an approximate time evolution of the spin system with a diagonalisation of the fermionic problem by Legendre expansion, and requires a much smaller number of MC accept-reject steps. However, this approach has the drawback of involving a molecular dynamics type simulation of the classical degrees of freedom, which is a bit complicated and which may bias the system in the direction of the assumed approximate dynamics.

Focussing on the problem of classical double-exchange, Eq. (111), we therefore proposed a third approach [77], which combines the advantages of KPM with the highly efficient Cluster MC algorithms [78, 79, 80]. In general, for a classical MC algorithm the transition probability from state a to state b can be written as

$$P(a \rightarrow b) = A(a \rightarrow b) \tilde{P}(a \rightarrow b), \quad (155)$$

where $A(a \rightarrow b)$ is the probability of *considering* the move $a \rightarrow b$, and $\tilde{P}(a \rightarrow b)$ is the probability of *accepting* the

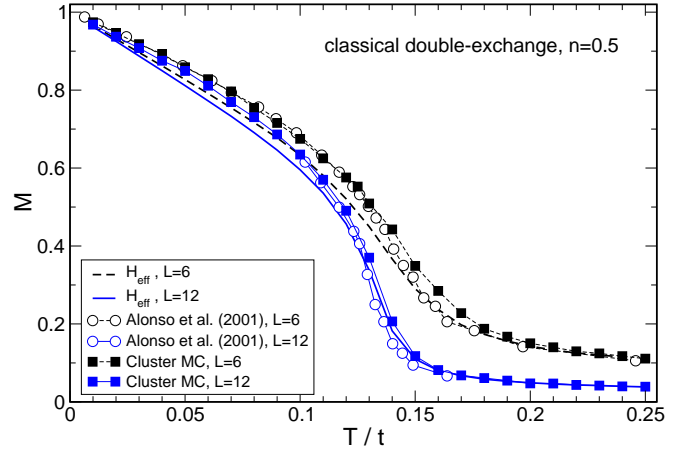


FIG. 12: Magnetisation as a function of temperature for the classical double-exchange model at doping $x = 0.5$. We compare data obtained from the effective model H_{eff} (see text), from a hybrid Monte Carlo approach [76], and from a KPM based Cluster Monte Carlo technique [77]. L denotes the size of the underlying three-dimensional cluster, i.e., $D = L^3$ is the dimension of the fermionic problem.

move $a \rightarrow b$. Given the Boltzmann weights of the states a and b , $W(a)$ and $W(b)$, detailed balance requires that

$$W(a)P(a \rightarrow b) = W(b)P(b \rightarrow a), \quad (156)$$

which can be fulfilled with a generalised Metropolis algorithm

$$\tilde{P}(a \rightarrow b) = \min \left(1, \frac{W(b)A(b \rightarrow a)}{W(a)A(a \rightarrow b)} \right). \quad (157)$$

In the standard MC approach for spin systems only a single randomly chosen spin is flipped. Hence, $A(a \rightarrow b) = A(b \rightarrow a)$ and the probability $\tilde{P}(a \rightarrow b)$ is usually much smaller than 1, since it depends on temperature via the weights $W(a)$ and $W(b)$. This disadvantage can be avoided by a clever construction of clusters of spins, which are flipped simultaneously, such that the *a priori* probabilities $A(a \rightarrow b)$ and $A(b \rightarrow a)$ soak up any difference in the weights $W(a)$ and $W(b)$. We then arrive at the famous rejection-free cluster MC algorithms [78], which are characterised by $\tilde{P}(a \rightarrow b) = 1$.

For the double-exchange model (111) we cannot expect to find an algorithm with $\tilde{P}(a \rightarrow b) = 1$, but even a method with $\tilde{P}(a \rightarrow b) = 0.5$ would be highly efficient. As is known, the amplitude of the hopping matrix element (112) is given by the cosine of half the relative angle between neighbouring spins, or $|t_{ij}|^2 = (1 + \vec{S}_i \cdot \vec{S}_j)/2$. Averaging over the fermionic degrees of freedom, we thus arrive at an effective classical spin model

$$H_{\text{eff}} = -J_{\text{eff}} \sum_{\langle ij \rangle} \sqrt{1 + \vec{S}_i \cdot \vec{S}_j}, \quad (158)$$

where the particle density n approximately defines the coupling, $J_{\text{eff}} \approx n(1 - n)/\sqrt{2}$. Similar to a classical

Heisenberg model, the Hamiltonian H_{eff} is a sum over contributions of single bonds, and we can therefore construct a cluster algorithm with $\tilde{P}(a \rightarrow b) = 1$. Surprisingly, the simulation of this pure spin model yields magnetisation data, which almost perfectly matches the results for the full classical double-exchange model at doping $n = 0.5$, see Figure 12.

For simulating the coupled spin fermion model (111) we suggested to apply the single cluster algorithm for H_{eff} until approximately every spin in the system has been flipped once, thereby keeping track of all *a priori* probabilities $A(a \rightarrow b)$ of subsequent cluster flips. Then for the new spin configuration the energy of the electron system is evaluated with the help of KPM. Note however, that for a reliable discrimination of H_{eff} and the full fermionic model (111) the energy calculation needs to be very precise. For the moment calculation we therefore relied on complete trace summations instead of stochastic estimates. The KPM step is thus no longer linear in D , but still much faster than a full diagonalisation of the bilinear fermionic model. Based on the resulting energy, the new spin configuration is accepted with the probability (157). Figure 12 shows the magnetisation of the double-exchange model as a function of temperature for $n = 0.5$. Except for small deviations near the critical temperature the data obtained with the new approach compares well with the results of the Hybrid MC approach [76], and due to the low numerical effort rather large systems can be studied.

Of course, the combination of KPM and classical Monte Carlo not only works for spin systems. We may also think of models involving the coupling of electronic degrees of freedom to adiabatic lattice distortions or other classical variables [75], and as yet the potential of such combined approaches is certainly not fully exhausted.

The next application, which makes use of KPM as a component of a more general numerical approach, brings us back to interacting quantum systems, in particular, correlated electron systems with strong local interactions.

B. Cluster Perturbation Theory (CPT)

1. General features of CPT

Earlier in this review we have demonstrated the advantages of the Chebyshev approach for the calculation of spectral functions, optical conductivities and structure factors of complicated interacting quantum systems. However, owing to the finite size of the considered systems, quantities like the spectral function $A(\vec{k}, \omega)$ could only be calculated for a finite set of independent momenta \vec{k} . The interpretation of this “discrete” data may sometimes be less convenient, e.g. the \vec{k} -integrated one-electron density $\rho(\omega) = \int dk^d A(\vec{k}, \omega)$ does not show bands but only discrete poles which are grouped to band

like structures. Although this does not substantially bias the interpretation it is desirable to restore the translational symmetry of the lattice and reintroduce an infinite momentum space.

With the Cluster Perturbation Theory (CPT) [81, 82, 83] a straightforward way to perform this task approximatively has recently been devised. To describe it in a nutshell, let us consider a model of interacting fermions on a one-dimensional chain

$$H = -t \sum_{i\sigma} (c_{i+1,\sigma}^\dagger c_{i,\sigma} + \text{H.c.}) + \sum_i U_i. \quad (159)$$

Here U_i denotes a local interaction, e.g. $U_i = U n_{i\uparrow} n_{i\downarrow}$ for the Hubbard model. CPT starts by breaking up the infinite system into short finite chains of L sites each (clusters), which all are equivalent due to translational symmetry. From the Green function of a finite chain, $G_{ij}^c(\omega)$ with $i, j = 0, \dots, L-1$, which is calculated exactly by a suitable numerical method, the Green function $G(k, \omega)$ of the infinite chain is obtained by re-introducing the hopping between the segments. This inter-chain hopping is treated on the level of a random phase approximation (RPA), which neglects correlations between different chains. The Green function $G_{ij}^{nm}(\omega)$ is then given through a Dyson equation

$$G_{ij}^{nm}(\omega) = \delta_{nm} G_{ij}^c(\omega) + \sum_{i', j', m'} G_{ii'}^c(\omega) V_{i'j'}^{nm'} G_{j'j}^{m'm}(\omega), \quad (160)$$

where $V_{ij}^{nm} = -t(\delta_{n,m+1} \delta_{i0} \delta_{j,L-1} + \delta_{n,m-1} \delta_{i,L-1} \delta_{j0})$ describes the inter-chain hopping and upper indices number the different clusters. A partial Fourier transform of the inter-chain hopping, $V_{ij}(Q) = -t(e^{iQ} \delta_{i0} \delta_{j,L-1} + e^{-iQ} \delta_{i,L-1} \delta_{j0})$, gives the infinite lattice Green function in a mixed representation

$$\hat{G}_{ij}(Q, \omega) = \left(\frac{G^c(\omega)}{1 - V(Q)G^c(\omega)} \right)_{ij} \quad (161)$$

for a momentum vector Q of the super-lattice of finite chains and cluster indices i, j . Finally, from this mixed representation the infinite lattice Green function in momentum space is recovered in the CPT approximation as a simple Fourier transform

$$G(k, \omega) = \frac{1}{L} \sum_{i,j} \exp(i(i-j)k) \hat{G}_{ij}(Lk, \omega). \quad (162)$$

The reader should be aware that restoring translational symmetry in the CPT sense is different from restoring the thermodynamic limit of the interacting system. The CPT may be understood as a kind of interpolation scheme from the discrete momentum space of a finite cluster to the continuous \vec{k} -values of the infinite lattice. The amount of information attainable from the solution of a finite cluster problem does however not increase. Especially finite size effects affecting the interaction properties are by no means reduced, but still determined

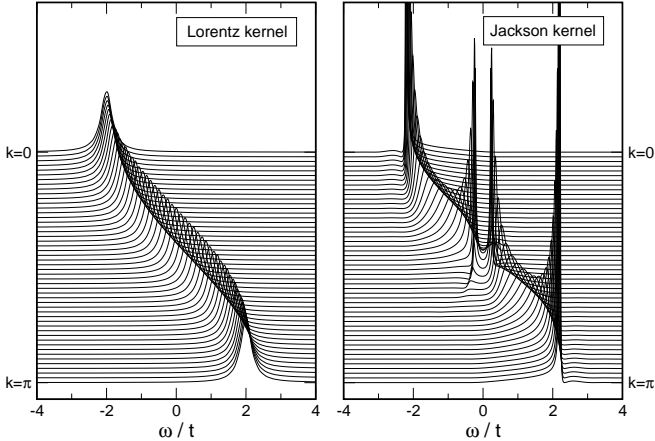


FIG. 13: Spectral function for non-interacting tight-binding electrons. Based on the Lorentz kernel CPT exactly reproduces the infinite system result (left), the Jackson kernel does not have the correct analytical properties, therefore CPT cannot close the finite size gap at $k = \pi/2$ (right).

through the size of the underlying cluster. Nevertheless, CPT yields appealing presentations of the finite cluster data, which can ease its interpretation.

At present, all numerical studies within the CPT context use Lanczos recursion for the cluster diagonalisation, thus suffering from the shortcomings we discussed earlier. As an alternative, we prefer to use the formalism introduced in section III B, which is much better suited for the calculation of spectral properties in a finite energy interval.

On applying the CPT crucial attention has to be paid to the kernel used in the reconstruction of $G_{ij}^c(\omega)$. As it turns out, the Jackson kernel is an inadequate choice here, since already for the non-interacting tight-binding model it introduces spurious structures into the spectra. The failure can be attributed to the shape of the Jackson kernel: Being optimised for high resolution, a pole in the Green function will give a sharp peak with most of its weight concentrated at the centre, and rapidly decaying tails. The reconstructed (cluster) Green function therefore does not satisfy the correct analytical properties required in the CPT step. To guarantee these properties, instead, we use the Lorentz kernel, which we constructed in section II C 3 to mimic the effect of a finite imaginary part in the energy argument of a Green function. Using this kernel for the reconstruction of $G_{ij}^c(\omega)$ the CPT works perfectly (cf. Figure 13).

To provide further examples we present results for two different interacting models where the cluster Green function $G_{ij}^c(\omega)$ has been calculated through a Chebyshev expansion as in Equation (120). Using $G_{ij}^c(\omega) = G_{ji}^c(\omega)$ (no magnetic field), for a L -site chain L diagonal and $L(L-1)/2$ off-diagonal elements of $G_{ij}^c(\omega)$ have to be calculated. Note also, that the latter can be reduced to Chebyshev iterations for the operators $c_i + c_j$, which allows application of the “doubling trick” (see the remark

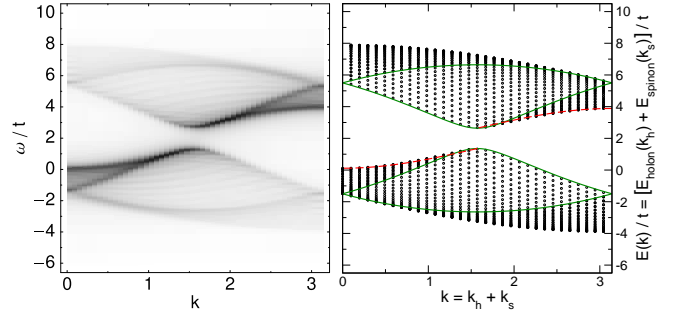


FIG. 14: Spectral function of the 1D Hubbard model at half-filling and with $U = 4t$. Left: CPT result for cluster size $L = 16$ and expansion order $N = 2048$. For similar data based on Lanczos recursion see Ref. 82. Right: Within the exact Bethe ansatz solution each electron separates into the sum of independent spinon (red dashed) and holon (green) excitations. The dots mark the energies of a 64-site chain.

after Equation (118)). However, if enough memory is available it is more efficient to keep the ground state of the system and to calculate L elements of $G_{ij}^c(\omega)$ in a single iteration. Remember that the cluster Green function is calculated for a chain with open boundary conditions. The reduced symmetry compared to periodic boundary conditions results in a larger dimension of the Hilbert space that has to be dealt with numerically.

2. CPT for the Hubbard model

As a first example we consider the 1D Hubbard model (Eq. (123) with $g = \omega_0 = 0$), which is exactly solvable by Bethe ansatz [84] thus providing the opportunity to assess the precision of the CPT. The left hand side of Figure 14 shows the one-particle spectral function at half-filling, calculated on the basis of $L = 16$ site clusters and an expansion order of $N = 2048$. The matrix dimension is $D \approx 1.7 \cdot 10^8$. On the right hand side the dots show the Bethe ansatz results for a $L = 64$ site chain, and the lines denote the $L \rightarrow \infty$ spinon and holon excitations each electron separates into (“spin-charge-separation”). Note that the Bethe ansatz does not allow for a direct calculation of the structure factor, the data thus represents only the position and density of the eigenstates, but is not weighted with the matrix elements of the operators $c_k^{(\dagger)}$. Although for an infinite system we would expect a continuous response, the CPT data shows some faint fine-structure. A comparison with the finite-size Bethe ansatz data reminds us that these features have their origin in the finite-cluster Greens function which the CPT spectral function is based on. Otherwise the CPT nicely reproduces all expected features, like the two pronounced spinon and holon branches and the excitation gap.

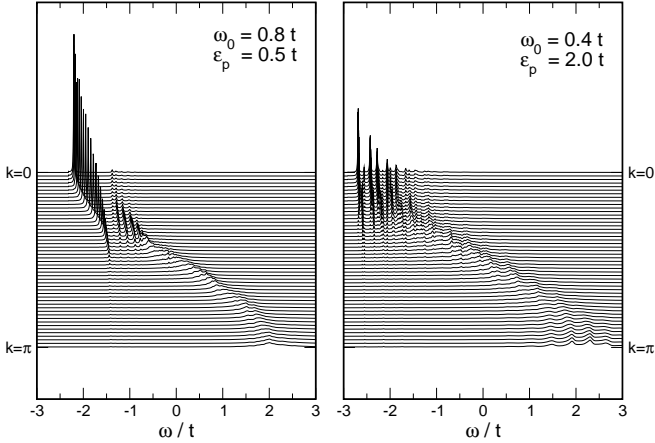


FIG. 15: Spectral function $A^+(k, \omega)$ of a single electron in the Holstein model (corresponding to $N_e = 0$ in Eq. (125)). For weak electron-phonon coupling the original band is still very pronounced (left), for intermediate-to-strong coupling many narrow polaron bands develop (right). The cluster size is $L = 16$ (left) or $L = 6$ (right) and the expansion order $N = 2048$. See Ref. 85 for similar data based on Lanczos recursion.

3. CPT for the Holstein model

Our second example is the spectral function of a single electron in the Holstein model, i.e., Eq. (123) with $U = 0$. Here, as a function of the electron-phonon interaction, polaron formation sets in and the band width of the resulting quasi particles becomes extremely narrow at large coupling strength. Figure 15 illustrates this behaviour for two values of the dimension-less coupling $\lambda = g^2 \omega_0 / (2t)$. For weak coupling the original one-electron band is still clearly visible, but the dispersionless phonon cuts in approximately at an energy ω_0 above the band minimum, causing an avoided-crossing like gap and a number of finite-size features. For strong coupling the spectral weight of the electron is distributed over many narrow polaron bands separated approximately by the bare phonon frequency ω_0 .

In all these cases, KPM works as a reliable high-resolution cluster solver, and using the concepts from section III D we could also extend these calculations to finite temperature. Probably, CPT is not the only approximate technique that profits from the simplicity and stability of KPM, and the range of its applications can certainly be extended.

V. OVERVIEW OF ALTERNATIVES TO KPM

After we have given a very detailed description of the Kernel Polynomial Method and presented a wide range of applications, let us now comment on a number of other numerical approaches that are closely related to KPM or compete with it.

A. Chebyshev expansion and Maximum Entropy methods

The first of these approaches, the combination of Chebyshev expansion and Maximum Entropy, is basically an alternative procedure to transform moment data μ_n into convergent approximations of the considered function $f(x)$. To achieve this, instead of applying kernel polynomials, an entropy

$$S(f, f_0) = \int_{-1}^1 (f(x) - f_0(x) - \log(f(x)/f_0(x))) dx \quad (163)$$

is maximised under the constraint that the moments of the estimated $f(x)$ agree with the given data. The function $f_0(x)$ describes our initial knowledge about $f(x)$, and may in the worst case just be a constant. Being related to Maximum Entropy approaches to the classical moment problem [86, 87], for the case of Chebyshev moments different implementations of the method have been suggested [38, 88, 89]. Since for a given set of N moments μ_n the approximation to the function $f(x)$ is usually not restricted to a polynomial of degree $N - 1$, compared to the KPM with Jackson kernel the Maximum Entropy approach usually yields estimates of higher resolution. However, the resource consumption of Maximum Entropy is generally much higher than the $N \log N$ behaviour we found for KPM. In addition, the approach is non-linear in the moments and can even become unstable for large N . Note also that as yet Maximum Entropy methods have been derived only for positive quantities, $f(x) > 0$, such as densities of states or strictly positive correlation functions.

Maximum Entropy, nevertheless, is a good alternative to KPM, if the calculation of the μ_n is particularly time consuming. Based on only a moderate number of moments it extracts the maximal information about $f(x)$, and we obtained very good results for some computationally demanding problems [59].

B. Lanczos recursion

The Lanczos Recursion Method is certainly the most capable competitor of the Kernel Polynomial Method [26]. It is based on the Lanczos algorithm [24], a method which was initially developed for the tridiagonalisation of Hermitian matrices and later evolved to one of the most powerful methods for the calculation of extremal eigenstates of sparse matrices [90]. Although ideas like the mapping of the classical moment problem to tridiagonal matrices and continued fractions have been suggested earlier [91], the use of the Lanczos algorithm for the characterisation of spectral densities [18, 19] was first proposed at about the same time as the Chebyshev expansion approaches, and in principle Lanczos recursion is also a kind of modified moment expansion [20, 21]. Its generalisation from spectral densities to zero temperature

Chebyshev / KPM	complexity	Lanczos recursion	complexity
Initialisation:	Initialisation:		
$\tilde{H} = (H - b)/a$		$\beta_0 = \sqrt{\langle 0 A^\dagger A 0 \rangle}$	
$ \phi_0\rangle = A 0\rangle, \quad \phi_1\rangle = \tilde{H} \phi_0\rangle$		$ \phi_0\rangle = A 0\rangle/\beta_0, \quad \phi_{-1}\rangle = 0$	
$\mu_0 = \langle \phi_0 \phi_0 \rangle, \quad \mu_1 = \langle \phi_1 \phi_0 \rangle$			
Recursion for $2N$ moments μ_n :	$O(ND)$	Recursion for N coefficients α_n, β_n :	$O(ND)$
$ \phi_{n+1}\rangle = 2\tilde{H} \phi_n\rangle - \phi_{n-1}\rangle$		$ \tilde{\phi}\rangle = H \phi_n\rangle - \beta_n \phi_{n-1}\rangle, \quad \alpha_n = \langle \phi_n \tilde{\phi} \rangle$	
$\mu_{2n+2} = 2\langle \phi_{n+1} \phi_{n+1} \rangle - \mu_0$		$ \tilde{\phi}\rangle = \tilde{\phi}\rangle - \alpha_n \phi_n\rangle, \quad \beta_{n+1} = \sqrt{\langle \tilde{\phi} \tilde{\phi} \rangle}$	
$\mu_{2n+1} = 2\langle \phi_{n+1} \phi_n \rangle - \mu_1$		$ \phi_{n+1}\rangle = \tilde{\phi}\rangle/\beta_{n+1}$	
→ very stable		→ tends to lose orthogonality	
Reconstruction in three simple steps:	$O(M \log M)$	Reconstruction via continued fraction	$O(NM)$
Apply kernel: $\tilde{\mu}_n = g_n \mu_n$		$f(z) = -\frac{1}{\pi} \operatorname{Im} \frac{\beta_0^2}{z - \alpha_0 - \frac{\beta_1^2}{z - \alpha_1 - \frac{\beta_2^2}{z - \alpha_2 - \dots}}}$	
Fourier transform: $\tilde{\mu}_n \rightarrow \tilde{f}(\tilde{\omega}_i)$			
Rescale: $f(w_i) = \frac{\tilde{f}[(\omega_i - b)/a]}{\pi \sqrt{a^2 - (\omega_i - b)^2}}$		where $z = \omega_i + i\epsilon$	
→ procedure is linear in μ_n		→ procedure is non-linear in α_n, β_n	
→ well defined resolution $\propto 1/N$		→ ϵ is somewhat arbitrary	

TABLE II: Comparison of Chebyshev expansion and Lanczos recursion for the calculation of a zero-temperature dynamical correlation function $f(\omega) = \sum_n |\langle n | A | 0 \rangle|^2 \delta(\omega - \omega_n)$. We assume N matrix vector multiplications with a D -dimensional sparse matrix H , and a reconstruction of $f(\omega)$ at M points ω_i .

dynamical correlation functions was first given in terms of continued fractions [92], and later also an approach based on the eigenstates of the tridiagonal matrix was introduced and termed Spectral Decoding Method [93]. This technique was then generalised to finite temperature [22, 28], and, in addition, some variants of the approach for low temperature [23] and based on the micro-canonical ensemble [94] have been proposed recently.

To give an impression, in Table II we compare the setup for the calculation of a zero temperature dynamical correlation function within the Chebyshev and the Lanczos approach. The most time consuming step for both methods is the recursive construction of a set of vectors $|\phi_n\rangle$, which in terms of scalar products yield the moments μ_n of the Chebyshev series or the elements α_n, β_n of the Lanczos tridiagonal matrix. In terms of the number of operations the Chebyshev recursion has a small advantage, but, of course, the application of the Hamiltonian as the dominant factor is the same for both methods. As a drawback, at high expansion order the Lanczos iteration tends to lose the orthogonality between the vectors $|\phi_n\rangle$, which it intends to establish by construction. When the Lanczos algorithm is applied to eigenvalue problems this loss of orthogonality usually signals the convergence

of extremal eigenstates, and the algorithm then starts to generate artificial copies of the converged states. For the calculation of spectral densities or correlation functions this means that the information content of the α_n and β_n does no longer increase proportionally to the number of iterations. Unfortunately, this deficiency can only be cured with more complex variants of the algorithm, which also increase the resource consumption. Chebyshev expansion is free from such defects, as there is a priori no orthogonality between the $|\phi_n\rangle$.

The reconstruction of the considered function from its moments μ_n or coefficients α_n, β_n , respectively, is also faster and simpler within the KPM, as it makes use of Fast Fourier Transformation. In addition, the KPM is a linear transformation of the moments μ_n , whereas continued fractions are non-linear in the coefficients α_n, β_n . A further advantage of KPM is our good understanding of its convergence and resolution as a function of the expansion order N . For the Lanczos algorithm these issues have not been worked out with the same rigour.

We therefore think that the Lanczos algorithm is an excellent tool for the calculation of extremal eigenstates of large sparse matrices, but for spectral densities and correlation functions the Kernel Polynomial Method is

the better choice. Of course, the advantages of both algorithms can be combined, e.g. when the Chebyshev expansion starts from an exact eigenstate that was calculated with the Lanczos algorithm.

C. Projection methods

Projection methods were developed mainly in the context of electronic structure calculations or tight-binding molecular dynamics, which both require knowledge of the total energy of a non-interacting electron systems or of related expectation values [27, 30]. The starting point of these methods is the density matrix $F = f(H)$, where $f(E)$ again represents the Fermi function. To obtain a set of thermally weighted states F is expanded as a polynomial in the Hamiltonian H and then applied to random vectors $|r\rangle$ or other basis states. Tracing or averaging over the thermally weighted states yields thermal expectation values, total energies or the like [29]. Usually, Chebyshev polynomials are the basis for the polynomial expansion of F [95], the approach is thus closely related to the KPM.

Of course, not only the fermionic density matrix but also its interacting equivalent, $\exp(-\beta H)$, can be expanded in polynomials, which leads to similar methods for interacting quantum systems. Recently a projection technique has also been suggested for dynamical correlation functions at finite temperature [31], where thermally weighted states are subjected to standard numerical time evolution and subsequent measurement of the considered correlation.

In terms of speed and resource consumption the projection methods are highly efficient and can be linear in the problem dimension D . However, in contrast to KPM they require a new simulation for each change in temperature or chemical potential, which represents their major disadvantage.

D. Forced Oscillator Method

Finally, let us comment on another approach that allows for the calculation of dynamical correlation functions and also has some relation to Chebyshev expansion. Introduced a couple of years ago for the study of phonon localisation [32], it is based on numerical time evolution. More precisely, a set of random phase vectors is subjected to a periodic force of frequency Ω , such that after a sufficient period of time the system arrives in a state whose energy E is very close to Ω . Thus, by changing Ω the spectral density and other properties of the eigenstates of energy E can be studied. Since the approach is already based on a periodic perturbation it can also be extended to yield zero-temperature dynamical correlation functions (see [96] for an extensive review). As a basic ingredient, the time evolution can be performed very efficiently on the basis of Chebyshev expansion, where now,

instead of the density matrix, the time evolution operator is expressed in terms of Chebyshev polynomials [9, 97].

Compared to KPM the Forced Oscillator Method is very complicated, since within one simulation only the response at a single frequency can be calculated and several convergence issues have to be taken into account. Moreover, it is restricted to zero temperature. Note also, that in the light of the KPM data we presented earlier the quality of the forced oscillator results published, e.g. for the spectral density and the optical response of the Anderson model [98, 99] is rather poor.

VI. CONCLUSIONS & OUTLOOK

In this review we gave a detailed introduction to the Kernel Polynomial Method, a numerical approach that on the basis of Chebyshev expansion allows for an efficient calculation of the spectral properties of large matrices and of the static and dynamic correlation functions, which depend on them. The method has a wide range of applications in different areas of physics and quantum chemistry, and we illustrated its capability with numerous examples from solid state physics, which covered such diverse topics as non-interacting electrons in disordered media, quantum spin models, or strongly correlated electron-phonon systems. Many of the considered quantities are hardly accessible with other methods, or could previously be studied only on smaller systems. Comparing with alternative numerical approaches, we demonstrated the advantages of KPM measured in terms of general applicability, speed, resource consumption, algorithmic simplicity and accuracy of the results.

Apart from further direct applications of the KPM outside the fields of solid state physics and quantum chemistry, we think that the combination of KPM with other numerical techniques will become one of the major future research directions. Certainly not only CPT and classical MC simulations, but potentially also other cluster approaches [100] or quantum MC can profit from the concepts outlined in this review.

Acknowledgements

We thank A. Basermann, B. Bäuml, M. Hohenadler, M. Kinateder, G. Schubert, and in particular R.N. Silver for fruitful discussions and technical support. Most of the calculations could only be performed with the generous grant of resources by the John von Neumann-Institute for Computing (NIC Jülich), the Leibniz-Rechenzentrum München (LRZ), the High Performance Computing Center Stuttgart (HLRS), the Norddeutscher Verbund für Hoch- und Höchstleistungsrechnen (HLRN), the Australian Partnership for Advanced Computing (APAC) and the Australian Centre for Advanced Computing and Communications (ac3). In addition, we are grateful for

support by the Australian Research Council and the Gor-

don Godfrey Bequest.

[1] W. Gautschi, *Math. Comp.* **22**, 251 (1968).

[2] W. Gautschi, *Math. Comp.* **24**, 245 (1970).

[3] R. A. Sack and A. F. Donovan, *Numer. Math.* **18**, 465 (1972).

[4] J. C. Wheeler and C. Blumstein, *Phys. Rev. B* **6**, 4380 (1972).

[5] C. Blumstein and J. C. Wheeler, *Phys. Rev. B* **8**, 1764 (1973).

[6] J. C. Wheeler, M. G. Prais, and C. Blumstein, *Phys. Rev. B* **10**, 2429 (1974).

[7] J. C. Wheeler, *Phys. Rev. A* **9**, 825 (1974).

[8] H. Tal-Ezer and R. Kosloff, *J. Chem. Phys.* **81**, 3967 (1984).

[9] R. Kosloff, *J. Phys. Chem.* **92**, 2087 (1988).

[10] V. A. Mandelshtam and H. S. Taylor, *J. Chem. Phys.* **107**, 6756 (1997).

[11] R. Chen and H. Guo, *Comp. Phys. Comm.* **119**, 19 (1999).

[12] D. Neuhauser, *J. Chem. Phys.* **93**, 2611 (1990).

[13] R. N. Silver and H. Röder, *Int. J. Mod. Phys. C* **5**, 935 (1994).

[14] L.-W. Wang and A. Zunger, *Phys. Rev. Lett.* **73**, 1039 (1994).

[15] L.-W. Wang, *Phys. Rev. B* **49**, 10154 (1994).

[16] R. N. Silver, H. Röder, A. F. Voter, and D. J. Kress, *J. of Comp. Phys.* **124**, 115 (1996).

[17] A. Weiße, *Eur. Phys. J. B* **40**, 125 (2004).

[18] R. Haydock, V. Heine, and M. J. Kelly, *J. Phys. C* **5**, 2845 (1972).

[19] R. Haydock, V. Heine, and M. J. Kelly, *J. Phys. C* **8**, 2591 (1975).

[20] P. Lambin and J.-P. Gaspard, *Phys. Rev. B* **26**, 4356 (1982).

[21] C. Benoit, E. Royer, and G. Poussigue, *J. Phys. Condens. Matter* **4**, 3125 (1992).

[22] J. Jaklič and P. Prelovšek, *Phys. Rev. B* **49**, 5065 (1994).

[23] M. Aichhorn, M. Daghofer, H. G. Evertz, and W. von der Linden, *Phys. Rev. B* **67**, 161103 (2003).

[24] C. Lanczos, *J. Res. Nat. Bur. Stand.* **45**, 255 (1950).

[25] S. T. Pantelides, *Rev. Mod. Phys.* **50**, 797 (1978).

[26] E. Dagotto, *Rev. Mod. Phys.* **66**, 763 (1994).

[27] P. Ordejón, *Comp. Mater. Sci.* **12**, 157 (1998).

[28] J. Jaklič and P. Prelovšek, *Adv. Phys.* **49**, 1 (2000).

[29] S. Goedecker and L. Colombo, *Phys. Rev. Lett.* **73**, 122 (1994).

[30] S. Goedecker, *Rev. Mod. Phys.* **71**, 1085 (1999).

[31] T. Iitaka and T. Ebisuzaki, *Phys. Rev. Lett.* **90**, 047203 (2003).

[32] M. L. Williams and H. J. Maris, *Phys. Rev. B* **31**, 4508 (1985).

[33] J. P. Boyd, *Chebyshev and Fourier Spectral Methods*, no. 49 in *Lecture Notes in Engineering*, Springer-Verlag, Berlin (1989).

[34] M. Abramowitz and I. A. Stegun (eds.), *Pocketbook of Mathematical Functions*, Verlag Harri Deutsch, Frankfurt/Main (1984).

[35] T. J. Rivlin, *Chebyshev polynomials: From Approximation Theory to Algebra and Number Theory*, Pure and Applied Mathematics, John Wiley & Sons, New York, 2 edn. (1990).

[36] E. W. Cheney, *Introduction to Approximation Theory*, McGraw-Hill, New York (1966).

[37] G. G. Lorentz, *Approximation of Functions*, Holt, Rinehart and Winston, New York (1966).

[38] J. Skilling, in J. Skilling (ed.), *Maximum Entropy and Bayesian Methods*, Fundamental Theories of Physics, pp. 455–466, Kluwer, Dordrecht (1988).

[39] D. A. Drabold and O. F. Sankey, *Phys. Rev. Lett.* **70**, 3631 (1993).

[40] T. Iitaka and T. Ebisuzaki, *Phys. Rev. E* **69**, 057701 (2004).

[41] D. Jackson, *Über die Genauigkeit der Annäherung stetiger Funktionen durch ganze rationale Funktionen gegebenen Grades und trigonometrische Summen gegebener Ordnung*, Ph.D. thesis, Georg-August-Universität Göttingen (1911).

[42] D. Jackson, *Trans. Amer. Math. Soc.* **13**, 491 (1912).

[43] C. Lanczos, *Discourse on Fourier series*, Hafner, New York (1966).

[44] M. Frigo and S. G. Johnson, FFTW fast fourier transform library, URL <http://www.fftw.org/>.

[45] P. W. Anderson, *Phys. Rev.* **109**, 1492 (1958).

[46] D. J. Thouless, *Physics Reports* **13**, 93 (1974).

[47] P. A. Lee and T. V. Ramakrishnan, *Rev. Mod. Phys.* **57**, 287 (1985).

[48] B. Kramer and A. Mac Kinnon, *Rep. Prog. Phys.* **56**, 1469 (1993).

[49] V. Dobrosavljević, A. A. Pastor, and B. K. Nikolić, *Europhys. Lett.* **62**, 76 (2003).

[50] G. Schubert, A. Weiße, and H. Fehske, URL <http://arXiv.org/abs/cond-mat/0309015>, preprint (2003).

[51] G. Schubert, A. Weiße, and H. Fehske, *Phys. Rev. B* **71**, 045126 (2005).

[52] K. Slevin and T. Ohtsuki, *Phys. Rev. Lett.* **82**, 382 (1999).

[53] P. W. Anderson and H. Hasegawa, *Phys. Rev.* **100**, 675 (1955).

[54] J. M. D. Coey, M. Viret, and S. von Molnár, *Adv. Phys.* **48**, 167 (1999).

[55] C. Zener, *Phys. Rev.* **82**, 403 (1951).

[56] A. Auerbach, *Interacting Electrons and Quantum Magnetism*, Graduate Texts in Contemporary Physics, Springer-Verlag, Heidelberg (1994).

[57] A. Weiße, J. Loos, and H. Fehske, *Phys. Rev. B* **64**, 054406 (2001).

[58] E. M. Kogan and M. I. Auslender, *Phys. Status Solidi B* **147**, 613 (1988).

[59] B. Bäuml, G. Wellein, and H. Fehske, *Phys. Rev. B* **58**, 3663 (1998).

[60] J. M. Robin, *Phys. Rev. B* **56**, 13634 (1997).

[61] S. Sykora, *et al.*, *Phys. Rev. B* **71**, 045112 (2005).

[62] M. Hohenadler, *et al.*, URL <http://arXiv.org/abs/cond-mat/0412010>, accepted for publication in *Phys. Rev. B* (2004).

- [63] H. Fehske, *et al.*, in S. Wagner, W. Hanke, A. Bode, and F. Durst (eds.), *High Performance Computing in Science and Engineering, Munich 2002*, pp. 339–350, Springer-Verlag, Heidelberg (2002).
- [64] H. Fehske, *et al.*, Phys. Rev. B **69**, 165115 (2004).
- [65] A. Weiße, G. Bouzerar, and H. Fehske, Eur. Phys. J. B **7**, 5 (1999).
- [66] A. W. Garrett, *et al.*, Phys. Rev. Lett. **79**, 745 (1997).
- [67] K. Fabricius and B. M. McCoy, Phys. Rev. B **59**, 381 (1999).
- [68] C. Schindelin, H. Fehske, H. Büttner, and D. Ihle, Phys. Rev. B **62**, 12141 (2000).
- [69] H. Fehske, *et al.*, Brazil. Jour. Phys. **30**, 720 (2000).
- [70] G. Schubert, *et al.*, in preparation.
- [71] Y. Motome and N. Furukawa, J. Phys. Soc. Jpn. **68**, 3853 (1999).
- [72] Y. Motome and N. Furukawa, J. Phys. Soc. Jpn. **69**, 3785 (2000).
- [73] Y. Motome and N. Furukawa, J. Phys. Soc. Jpn. **70**, 3186 (2001), erratum.
- [74] N. Furukawa and Y. Motome, J. Phys. Soc. Jpn. **73**, 1482 (2004).
- [75] G. Alvarez, *et al.*, URL <http://arXiv.org/abs/cond-mat/0502461>, preprint (2005).
- [76] J. L. Alonso, *et al.*, Nucl. Phys. B **596**, 587 (2001).
- [77] A. Weiße, H. Fehske, and D. Ihle, URL <http://arXiv.org/abs/cond-mat/0406049>, accepted for publication in Physica B (2004).
- [78] U. Wolff, Phys. Rev. Lett. **62**, 361 (1989).
- [79] W. Janke, Math. and Comput. in Simul. **47**, 329 (1998).
- [80] W. Krauth, in A. K. Hartmann and H. Rieger (eds.), *New Optimization Algorithms in Physics*, chap. 2, pp. 7–22, Wiley-VCH, Berlin (2004).
- [81] C. Gros and R. Valentí, Ann. Phys. (Leipzig) **3**, 460 (1994).
- [82] D. Sénéchal, D. Perez, and M. Pioro-Ladrière, Phys. Rev. Lett. **84**, 522 (2000).
- [83] D. Sénéchal, D. Perez, and D. Plouffe, Phys. Rev. B **66**, 075129 (2002).
- [84] F. H. L. Essler, *et al.*, *The One-Dimensional Hubbard Model*, Cambridge University Press, Cambridge (2005).
- [85] M. Hohenadler, M. Aichhorn, and W. von der Linden, Phys. Rev. B **68**, 184304 (2003).
- [86] L. R. Mead and N. Papanicolaou, J. Math. Phys. **25**, 2404 (1984).
- [87] I. Turek, J. Phys. C **21**, 3251 (1988).
- [88] R. N. Silver and H. Röder, Phys. Rev. E **56**, 4822 (1997).
- [89] K. Bandyopadhyay, A.K.Bhattacharya, P. Biswas, and D.A.Drabold, URL <http://arXiv.org/abs/cond-mat/0412717>, preprint (2004).
- [90] J. K. Cullum and R. A. Willoughby, *Lanczos Algorithms for Large Symmetric Eigenvalue Computations*, vol. I & II, Birkhäuser, Boston (1985).
- [91] R. G. Gordon, J. Math. Phys. **9**, 655 (1968).
- [92] E. Gagliano and C. Balseiro, Phys. Rev. Lett. **59**, 2999 (1987).
- [93] Q. Zhong, S. Sorella, and A. Parola, Phys. Rev. B **49**, 6408 (1994).
- [94] M. W. Long, *et al.*, Phys. Rev. B **68**, 235106 (2003).
- [95] S. Goedecker and M. Teter, Phys. Rev. B **51**, 9455 (1995).
- [96] T. Nakayama and K. Yakubo, Physics Reports **349**, 239 (2001).
- [97] V. V. Dobrovitski and H. De Raedt, Phys. Rev. E **67**, 056702 (2003).
- [98] T. Nakayama and H. Shima, Phys. Rev. E **58**, 3984 (1998).
- [99] H. Shima and T. Nakayama, Phys. Rev. B **60**, 14066 (1999).
- [100] T. Maier, M. Jarrell, T. Pruschke, and M. Hettler, URL <http://arXiv.org/abs/cond-mat/0404055>, preprint (2004).